TITLE PAGE

Immunocompetent Cell Targeting by Food-Additive Titanium Dioxide

Authors:

John W. Wills[1*], Alicja Dabrowska[1], Jack Robertson[1], Michelle Miniter[1], Sebastian Riedle[2,3], Huw D. Summers[4], Rachel E. Hewitt[1], Adeeba Fathima[1], Alessandra Barreto da Silva[1], Carlos A. P. Bastos[1], Stuart Micklethwaite[5], Åsa V. Keita[6], Johan D. Söderholm[6], Nicole C. Roy[2,7,8], Don Otter[9], Ravin Jugdaohsingh[1], Pietro Mastroeni[1], Andy P. Brown[3], Paul Rees[2], Jonathan J. Powell[1*].

Affiliations:

[1]Department of Veterinary Medicine, University of Cambridge, Cambridge CB3 0ES, UK.

[2]Riddet Institute, Massey University, Private Bag 11222, Palmerston North, 4442, New Zealand.

[3]Food Nutrition & Health Team, Food & Bio-based Products Group, AgResearch, Grasslands Research Centre, Tennent Drive, Private Bag 11008, Palmerston North, 4442, New Zealand.

[4]Department of Biomedical Engineering, Faculty of Science and Engineering, Swansea University, Swansea SA1 8EN, UK.

[5]School of Chemical and Process Engineering, University of Leeds, Leeds, LS2 9JT, UK.

[6]Department of Surgery and Department of Biomedical and Clinical Sciences, Linköping University, 58185 Linköping, Sweden.

[7]Department of Human Nutrition, University of Otago, Dunedin 9016, New Zealand.

[8]High-Value Nutrition Ko Ngā Kai Whai Painga National Science Challenge, Auckland 1142, New Zealand.

[9]Department of Food Science and Microbiology, Auckland University of Technology, Auckland, 1001, New Zealand.

***Joint-corresponding authors:**

John W. Wills & Jonathan J. Powell

Email: jw2020@cam.ac.uk / jjp37@cam.ac.uk
Tel: +44 (0)1223 337701
Biomineral Research, Department of Veterinary Medicine, School of Biological Sciences, University of Cambridge, Madingley Road, Cambridge CB3 0ES, UK.

ABSTRACT

Food-grade titanium dioxide ($fgTiO_2$) is a bio-persistent particle under intense regulatory scrutiny. Paradoxically, meaningful *in vivo* cellular accumulation has never been demonstrated: the only known cell reservoirs for $fgTiO_2$ are 'graveyard' intestinal pigment cells which are metabolically and immunologically quiescent. Here we identify major new immunocompetent cell targets of $fgTiO_2$ in humans, most notably in the subepithelial dome region of intestinal Peyer's patches. Using multimodal microscopy techniques with single-particle detection and per-cell / vesicle image analysis we achieved correlative dosimetry, quantitatively recapitulating human cellular exposures in the terminal ileum of mice fed a $fgTiO_2$-containing diet. Epithelial microfold cells selectively funneled $fgTiO_2$ into LysoMac and LysoDC cells with ensuing accumulation. Notwithstanding, proximity extension analyses for 92 protein targets revealed no measureable perturbation of cell signalling pathways. When chased with oral Δ*aroA*-*Salmonella*, pro-inflammatory signalling was confirmed, but no augmentation by $fgTiO_2$ was revealed despite marked same-cell loading. Interestingly, *Salmonella* caused the $fgTiO_2$-recipient cells to migrate basolaterally in the patch and, sporadically, to the lamina propria, thereby fully recreating the intestinal tissue distribution of $fgTiO_2$ in humans. Immunocompetent cells that accumulate $fgTiO_2$ *in vivo* are now identified and we demonstrate a mouse model that finally enables human-relevant risk assessments of ingested, bio-persistent (nano)particles.

54 **INTRODUCTION**

55 Titanium dioxide (TiO_2) is a highly versatile nano- and micro- particulate mineral with widespread
56 use in consumer products and manufacturing processes, including as a food and pharmaceutical
57 additive. Although, for many years[1, 2], there have been question marks over a potential role of
58 ingested TiO_2 in initiating or augmenting an inflammatory response in the intestine, the global
59 industry, valued at >$17 billion per annum[3], is now facing a whole new 'bio-nano' challenge. In May
60 2021, the European Food Safety Authority (EFSA) questioned the safety of food-grade TiO_2 ($fgTiO_2$;
61 also termed E171) primarily citing unresolved genotoxicity concerns[4]. Based on this, European
62 Commission member states agreed to remove $fgTiO_2$ as an additive in foods. This represented a
63 seemingly pragmatic decision balancing need for this additive (*e.g.,* aesthetics) against hypothetical
64 risk. However, the European Commission also requested that the European Medicines Agency
65 (EMA) evaluate the impact of removal of $fgTiO_2$ from the list of authorised excipients that are
66 permitted in medicinal products. In this case, $fgTiO_2$ is *not* merely about aesthetics: it delivers
67 opacity and protects actives from UV light degradation whilst aiding moisture control and patient
68 compliance. The EMA concluded that any foreseeable ban, impacting the ~91,000 medicinal
69 products that contain this pigment in Europe, risks causing pharmaceutical shortages[5]. Moreover,
70 they estimated that a period of 7-12 years would likely be required for implementation of suitable
71 alternatives[5]. Meanwhile, consumer concerns over the safety of $fgTiO_2$ have been expressed beyond
72 Europe. Notably, in 2022, a class action suit was filed against the multinational food company Mars
73 Incorporated in the USA alleging that consumers of the hard-shell candy 'Skittles' are at heightened
74 risk of health effects stemming from genotoxicity[6].

75

76 Whilst regulators in other continents / territories have not followed EFSA's 2021 decision, there is
77 widespread agreement that the available data addressing the uptake, biological fate and effects of
78 $fgTiO_2$ is insufficient[7, 8, 9]. In fact, direct toxicity of $fgTiO_2$ in cell culture experiments has not been

consistently demonstrated, especially when conditions are carefully controlled to avoid artefactual *in vitro* cell gorging[10]. In contrast, it is recognised *in vitro* that $fgTiO_2$ can modestly augment cellular responses to primary danger signals (*e.g.,* microbe-associated molecular patterns) although cell loading of the particles needs to be relatively high[1]. Similarly, Kirkland *et al.,*[11] identified any potential genotoxic activity of various titanium dioxide polymorphs as secondary to cell stress which, certainly for $fgTiO_2$, requires marked cell loading[1].

Aside from specific cells of the small intestine, there are no known circumstances under which $fgTiO_2$ markedly accumulates *in vivo*. Systemic exposure to $fgTiO_2$ appears to be very low[12]. Even allowing for lifetime accumulation in humans it appears that anticipated target organs (liver and spleen) contain levels of Ti and Ti-rich particulates that are just above the tissue-free background, and the origin of this slightly enhanced signal is unknown[13]. Consistent with this, many animal feeding studies show almost no detectable systemic accumulation of $fgTiO_2$[12, 14] and, overall, there are no convincing *ex vivo* imaging studies showing multiple, heavily-loaded cells. The exception, as noted above, is the small intestine, in both humans and rodent models[15, 16], and specifically their large lymphoid follicles termed Peyer's patches. In absence of afferent lymphatics, the apical surfaces of these follicles possess a unique population of microfold (M) cells that avidly sample the lumen for bulky macromolecules including small micro- and large nano- particles (herein referred to as 'particles'). This material is passed to underlying immune cells in the apical, 'subepithelial dome' (SED) region of the follicle which contains recognised populations of monocyte-derived, lysozyme-expressing cells termed 'LysoMacs' and 'LysoDCs' that are specialised for anti-microbial defence[17]. Overall, the major role of Peyer's patches is initiating processes for the generation of mucosal IgA and systemic IgG in response to intestinal antigen thereby orchestrating the sequence of events that leads to gut-derived humoral immunity. Over time, $fgTiO_2$ is known to accumulate in Peyer's patches, alongside other persistent particles, in basally located tissue-fixed macrophages termed

104 ‘pigment cells’[15, 16]. These cells are of low immunological and metabolic activity and appear to act as
105 lifetime ‘graveyards’ for persistent particles, presumably limiting systemic absorption through local
106 sequestration in the same way that tissue-fixed macrophages sequester particulate tattoo inks[15, 16, 18,
107 19].
108
109 So the paradox remains: whilst $fgTiO_2$ is under intense regulatory scrutiny, there is no known site of
110 accumulation in active (*e.g.,* immuno-competent) cells that could plausibly give cause for concern or
111 that allows informed risk assessment. Given that the intestine is the only known target of $fgTiO_2$
112 accumulation we have addressed whether similar, selective cell loading occurs elsewhere (*i.e.,* away
113 from the ‘safe house’ base-of-patch pigment cells) and, if so, what cells are targeted, at what
114 frequency and with what impact? The approach used quantitative image analysis of light and
115 electron microanalytical data, correlative mouse-human cell dosimetry and broad-target interrogation
116 of $fgTiO_2$’s capability to augment a primary cellular danger signal *in vivo*.
117
118 **RESULTS**
119 **Titanium dioxide in human intestinal tissues.** High-resolution reflectance confocal microscopy of
120 human small intestinal tissue samples identified bright foci at the base of Peyer’s patches (**Figure**
121 **1a)** consistent with previous reports of pigment cells in this region[16, 18, 20]. These cells are known to
122 mostly accumulate ingested engineered aluminosilicates and $fgTiO_2$[16, 20]. Using Al and Ti as
123 biomarkers for these particles, correlative analyses using scanning electron microscopy (SEM) and
124 energy dispersive X-ray spectroscopy (EDX) confirmed the presence and co-localisation of these
125 elements (**Figure 1b**; top row). Reflectant foci were found entirely attributable to Ti-rich particles, as
126 areas with Al but no Ti signals were not reflectant, whereas all detectable Ti foci yielded reflectance
127 (**Figure 1b**; rows 2-5). Alongside further checks using mouse tissues known to contain $fgTiO_2$ or not

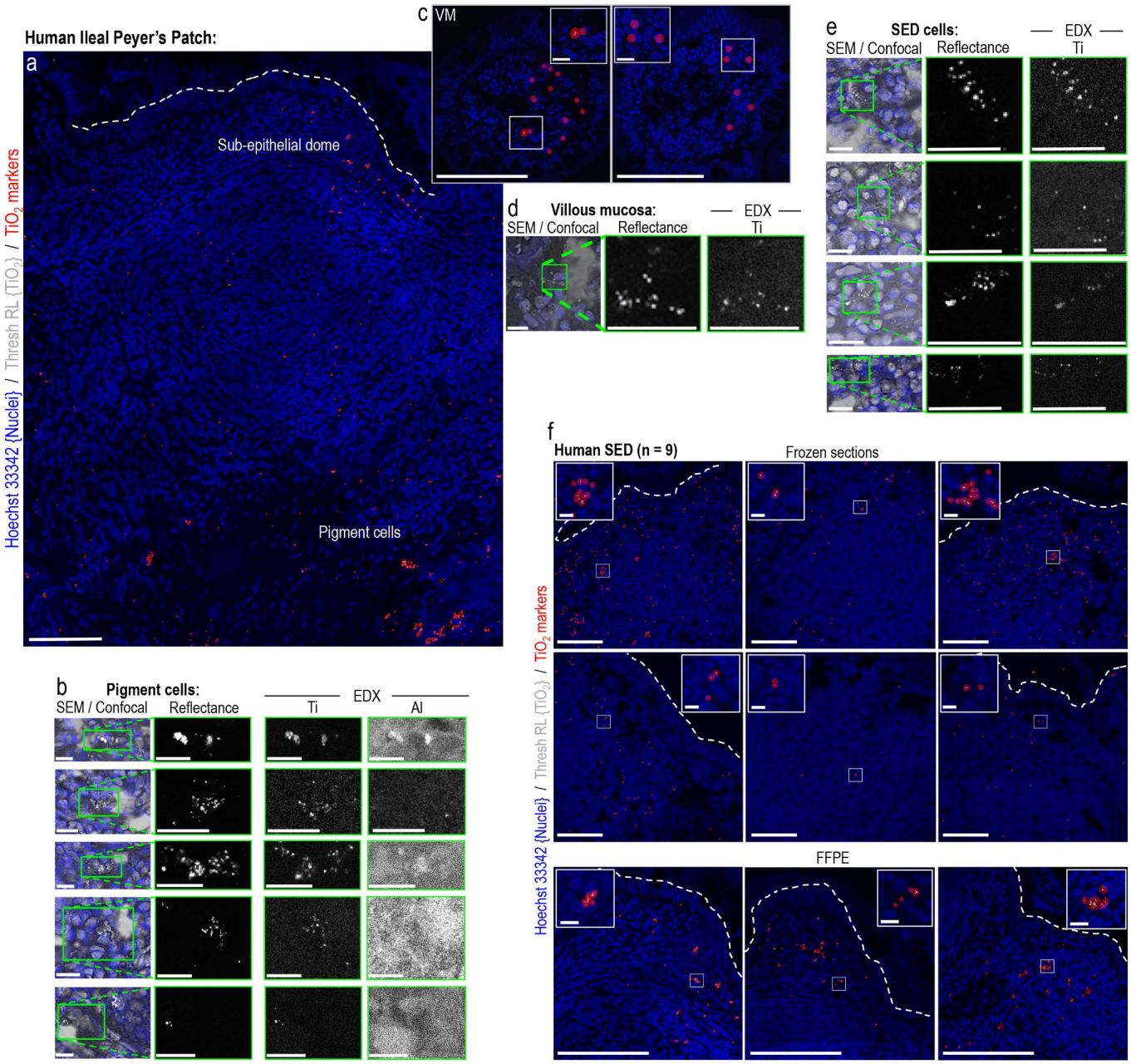

Figure 1 – Titanium dioxide in human intestinal tissues. a, Tilescanned image acquired by confocal reflectance microscopy. Reflectant foci were detected along the follicle base consistent with previously-reported mineral particle-containing "pigment cells". Of note, similar reflectant foci were also present apically in the immuno-active, subepithelial dome tissue-region, and away from the patch in the (**c**) lamina propria of the regular villous mucosa (VM). Translucent red circle-markers are placed on the reflectant foci to aid visualisation. **b**/**d**/**e**, Correlative SEM/EDX analyses performed on the same tissue section shown in (**a**/**c**). The pigment cell region is shown in (**b**) where X-ray signal for both Al (attributable to aluminosilicates) and Ti (attributable to titanium dioxide) was found. EDX analyses in the (**d**) villous mucosa and (**e**) subepithelial dome regions showed reflectant foci were attributable to Ti. **b**/**d**/**e**, In all instances the elemental data for Ti were a near-exact match for the reflectant foci, whereas (**b**) areas with Al signal alone did not reflect. **f**, Reflectance microscopical analyses of nine, randomly-drawn human samples (six frozen, three formalin-fixed paraffin embedded (FFPE)) showed reflectant foci consistent with TiO_2 in the subepithelial dome of *every* sample. *Scale bars:* ***a*** *= 50 µm;* ***b*** *= 50 µm with 10 µm insets;* ***c-e*** *= 10 µm;* ***f*** *= 50 µm with 10 µm insets.*

128 (shown, **Supplementary Figure 1**), the reflectance imaging approach was confirmed as a robust,
129 high-throughput means to detect $fgTiO_2$ in tissue[15].
130
131 Of significant note, previously unreported populations of human cells containing similar, reflective
132 material were also identified (i) sporadically in the regular lamina propria (**Figure 1c**) and (ii)
133 densely in the immuno-active subepithelial dome (SED) region of Peyer's patches (**Figure 1a**).
134 These cell regions were also subjected to correlative SEM-EDX analyses and, again, reflectant foci
135 were a match for the Ti signal (**Figure 1d/e**). Given the unexpected density of the newly-identified
136 Peyer's patch population, whole SED regions from a randomly selected series of nine human
137 subjects were imaged using the analytically-validated confocal microscopy approach. Albeit with
138 marked inter-individual variability, reflectant signal was found in the SED of every human case
139 (**Figure 1f**). Importantly, the recipient cells often exhibited multiple foci per-cell (*i.e.,* high cellular
140 loading), suggesting specific cellular targeting and accumulation of $fgTiO_2$ (**Figure 1f** – insets) in a
141 non-pigment cell population.
142
143 **Recapitulation in a mouse model.** To investigate the pathways giving rise to the above
144 observations, and to phenotype the newly-identified population of $fgTiO_2$-accumulating cells, in
145 "Mouse Study 1", we turned to a recently reported murine model for human-relevant, oral exposure
146 to $fgTiO_2$[15]. Initially we tilescanned a complete ileal transverse section using high-resolution
147 confocal reflectance microscopy and used image analysis to segment all cells (cell segmentation
148 accuracies assessed, **Supplementary Figure 2**). This allowed the cellular dose of $fgTiO_2$ to be
149 measured in each cell-object (*i.e.,* the integrated intensity of the thresholded reflectance signal per
150 cell) enabling the subdivision and display of the cellular loading of $fgTiO_2$ in three groups: low,
151 intermediate and high (**Figure 2a**). As in the human samples (**Figure 1**), the patch region was
152 decorated with reflectance signal, notably in the SED and at the base, and cellular loading was often

153 high – especially in the SED (**Figure 2a**). However, unlike in human tissue, signal was entirely
154 absent away from the patch except for two small, isolated foci in the villous epithelium. The
155 resolution of the imaging process allowed detailed investigation of these latter events confirming that
156 this signal was not *inside* the tissue, but derived from material within goblet cell invaginations that
157 were open to the intestinal lumen (**Figure 2a** – inset).
158
159 To confirm the apparent selectivity of $fgTiO_2$ for the lymphoid follicles – rather than the regular
160 villous mucosa – we questioned whether a single particle in intestinal tissue would be missed by our
161 reflectance microscopy approach. To do this, a tissue region containing a single, small yet clearly
162 visible reflectant foci was milled out under correlative SEM, using a focussed ion beam (**Figure 2b-**
163 **d**). The milled-out lamella was then transferred to a transmission electron microscope for imaging
164 with analysis by EDX and electron diffraction. A single particle of $fgTiO_2$, with a diameter around
165 100 nm and an anatase diffraction pattern consistent with dietary exposure, was identified (**Figure**
166 **2e-i**). Since single, disperse particles of $fgTiO_2$ were therefore detectable by the reflectance imaging
167 strategy we could confirm that ingested $fgTiO_2$ had not been missed with our imaging approach in
168 the regular villous mucosa and thus was not taken up in this region (**Figure 2a**).
169
170 Following from this, we next considered the caecal patches (*i.e.,* large lymphoid follicles of the first
171 part of the large intestine that adjoins the terminal ileum where Peyer's patches are located). Here,
172 transverse tissue sections revealed almost no reflectant foci showing that, unlike Peyer's patches, the
173 neighbouring caecal patch is spared from particle targeting (**Figure 2j**). In spite of the marked
174 similarity of these secondary lymphoid sites, the microfold (M) cell density of their overlying
175 epithelium differs greatly: caecal patches have very few (like the villous epithelium) with little
176 capacity for particle uptake, whereas Peyer's patch epithelium is enriched with mature M-cells that
177 exhibit distinct particle uptake capability for small particulates in general[21, 22]. Indeed, cells of the

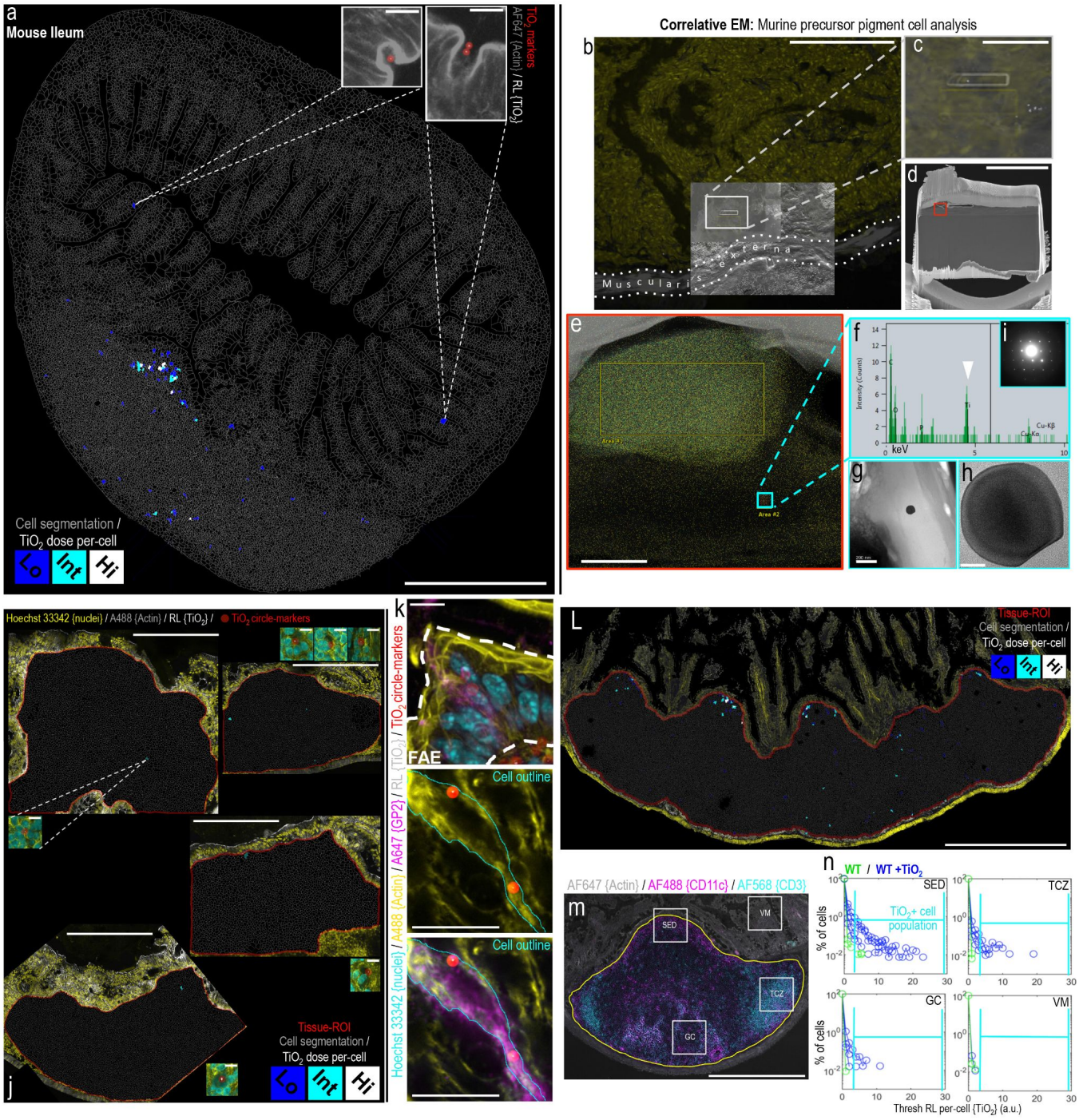

Figure 2 – A mouse feeding study demonstrates $fgTiO_2$ specificity for Peyer's patches. a, Single-cell image analysis of a transverse mouse ileal tissue section imaged by tilescanning confocal reflectance microscopy. The cellular dose of $fgTiO_2$ – measured from the thresholded reflectance (RL) signal – is colour-coded at low (lo), intermediate (int) and high (hi) levels. As in humans (**Figure 1a/f**), $fgTiO_2$ loaded into the subepithelial dome of the Peyer's patch and there was evidence of 'precursor pigment cell' formation along the follicle base. Away from the Peyer's patch, two positive cells (**a**, insets) were found in the overlying villous mucosa. In contrast to the human findings (**Figure 1c**) however, both were caused by luminal $fgTiO_2$ trapped in the invaginated space of goblet cells. **b-d**, To investigate the sensitivity of $fgTiO_2$ detection by confocal reflectance microscopy, a tissue-region containing a single, isolated reflectant foci was milled out under correlative SEM using a focussed ion beam (**b/c** shows the registered SEM images transparently overlaid onto the confocal reflectance data before lift-out. The white 'rectangle' in (**c**) is caused by electron charging of the platinum strap laid down on the tissue region to be lifted out; (**d**) shows a side-view of the lifted-out lamella). **e-i**, Transfer of the lamella to a transmission electron microscope enabled high resolution imaging and X-ray (EDX) and electron diffraction analysis. A (**g/h**) single particle of $fgTiO_2$ with an (**i**) anatase diffraction pattern (*i.e.,* as added to the diet) was confirmed responsible for the single reflectant foci observed. **j**, Again, colour-coding the cellular dose of $fgTiO_2$ into lo, int and hi levels, tissue sections from adjacent caecal patches at the top of the colon were found to be almost completely devoid of $fgTiO_2$ (n = 4 animals). **k**, Immunofluorescence microscopy showed $fgTiO_2$ access to Peyer's patches was via GP2-positive microfold (M) cells (translucent red circle-markers are placed on thresholded reflectant foci to aid $fgTiO_2$ visualisation / the outline of the M-cell was manually drawn by tracing the actin-delineated cell boundary). **L**, Single-cell analysis of a longitudinal section of mouse ileum consistently showed the close association between an M-cell rich, follicle-associated epithelium and $fgTiO_2$ loading into Peyer's patches. **m/n**, Guided by CD11c and CD3 immunofluorescence labelling for phagocytic mononuclear cells and T-lymphocytes (respectively) sets of images were collected from the subepithelial dome (SED), germinal centre (GC) T-cell zone (TCZ) or overlying villous mucosa (VM) tissue regions from four mice fed the $fgTiO_2$-supplemented diet (WT + TiO_2) and four control-diet mice (WT). Some $fgTiO_2$ signal was observed in the GC and TCZ regions of the murine Peyer's patches but the majority was in the SED. In keeping with (**a**), and in contrast to the human findings (**Figure 1c**), in all four mice, no uptake was seen in the villous mucosa demonstrating specificity for M-cell mediated, Peyer's patch targeting. *Scale bars:* ***a*** *= 500 µm with insets 5 µm;* ***b*** *= 50 µm;* ***c*** *= 10 µm;* ***d*** *= 5 µm;* ***e*** *= 500 nm;* ***g*** *= 200 nm;* ***h*** *= 20 nm;* ***j*** *= 500 µm;* ***k*** *= 10 µm;* ***L/m*** *= 500 µm.*

178 Peyer's patch epithelium stained positively for the mature M-cell marker (GP2) and, here-and-there,
179 these M-cells were 'caught in the act' with co-signal for $fgTiO_2$ (**Figure 2k**) as had long been
180 assumed for $fgTiO_2$ but not actually demonstrated[18]. Indeed, longitudinal sections of ileal tissue
181 containing Peyer's patches consistently demonstrated the close association between $fgTiO_2$ signal
182 and an overlying, M-cell rich, follicle-associated epithelium (**Figure 2L**). In this way, the above
183 findings provide a rationale for the specificity of $fgTiO_2$ uptake by the Peyer's patches of the small
184 intestine. It would appear, therefore, that to explain the presence of $fgTiO_2$ in the human intestinal
185 lamina propria a mechanism other than direct uptake by the regular villous epithelium must exist
186 (this is addressed below in "Mouse Study 2"). First, however, we quantified how cell loading with
187 $fgTiO_2$ varied amongst the major different functional zones of the Peyer's patch.
188
189 Sets of confocal reflectance images were collected from the SED, germinal centre (GC), T-cell zone
190 (TCZ) and overlying villous mucosa (VM) tissue regions (indicated, **Figure 2m**) using tissue
191 sections taken from four mice fed with the $fgTiO_2$-supplemented diet (+$fgTiO_2$), alongside four
192 control mice from the same experiment and ingesting the same diet but without added $fgTiO_2$.
193 Single-cell analysis, using flow cytometry-type gating informed by the negative control tissues,
194 demonstrated some $fgTiO_2$ signal in the TCZ and GC but established the dominance of the signal,
195 and the highest cell loading, in the biologically-active SED (**Figure 2n**). As per the whole ileal
196 cross-section data (**Figure 2a**), in all sections analysed across the four mice, the villous mucosa was
197 entirely devoid of $fgTiO_2$-positive cells and consistently exhibited the same reflectance distribution
198 as the negative control mice (**Figure 2n**).
199
200 **Establishing correlative human-mouse dosimetry.** Rodent models provide pragmatic access to
201 healthy pristine tissue (*i.e.,* rapidly flash frozen at necropsy) from fully controlled experiments (*i.e.,*
202 population-matched with availability of $fgTiO_2$-negative tissues) in a way that human surgical

203 specimens do not. Nonetheless, it is critical that a murine feeding model appropriately reports on the
204 human situation. Next, therefore, we exploited the window-of-insight provided by precision image
205 analysis to consider how the cellular dosimetry of $fgTiO_2$ in the SED cells of the murine model
206 reflected SED-cell exposure in humans. To do this, the snap-frozen Peyer's patch tissue sections,
207 taken from six randomly-drawn human samples, were compared with six murine samples taken from
208 the $fgTiO_2$-fed group. Visually, in both species, there was marked inter-individual variability in
209 $fgTiO_2$ concentration in the SED (**Figure 3a-L**). To quantify this, we analysed the thresholded
210 reflectance signal in the tissue sections in four ways, namely: thresholded reflectance per unit tissue
211 area (*i.e.,* $fgTiO_2$ abundance; **Figure 3m),** thresholded reflectance per cell (*i.e.,* $fgTiO_2$ load per cell;
212 **Figure 3n**), the number of reflectant foci per cell (*i.e.,* cellular count of $fgTiO_2$-loaded vesicles;
213 **Figure 3o**), and finally the amount of reflectance signal per foci (*i.e.,* $fgTiO_2$ load per vesicle;
214 **Figure 3p)**. The strategy is schematically explained in **Supplementary Figure 3**; cell segmentation
215 accuracy assessments are presented in **Supplementary Figure 2**; background reflectance
216 comparisons in mice and humans are shown in **Supplementary Figure 4** and examples of the raw
217 reflectance signal, resulting circle-marker placements and $fgTiO_2$-loaded vesicle segmentations are
218 shown in **Supplementary Figure 5**. By all metrics, the data from the two groups showed remarkable
219 overlap and under statistical comparison none of the measured $fgTiO_2$ distributions were found to be
220 entirely unique to either species (presented, **Supplementary Figure 6**). Notably when Peyer's patch
221 loading of $fgTiO_2$ from mice on lower-dose-$fgTiO_2$ diets was analysed, the cellular accumulation of
222 particles in the SED was several orders of magnitude lower compared to the human situation
223 (**Supplementary Figure 7**). The above findings therefore establish the apparent ability of the murine
224 model to provide human-relevant data – quantitatively as well as qualitatively – in terms of $fgTiO_2$
225 cell targeting and dosimetry in the biologically-active SED region of the Peyer's patch.
226

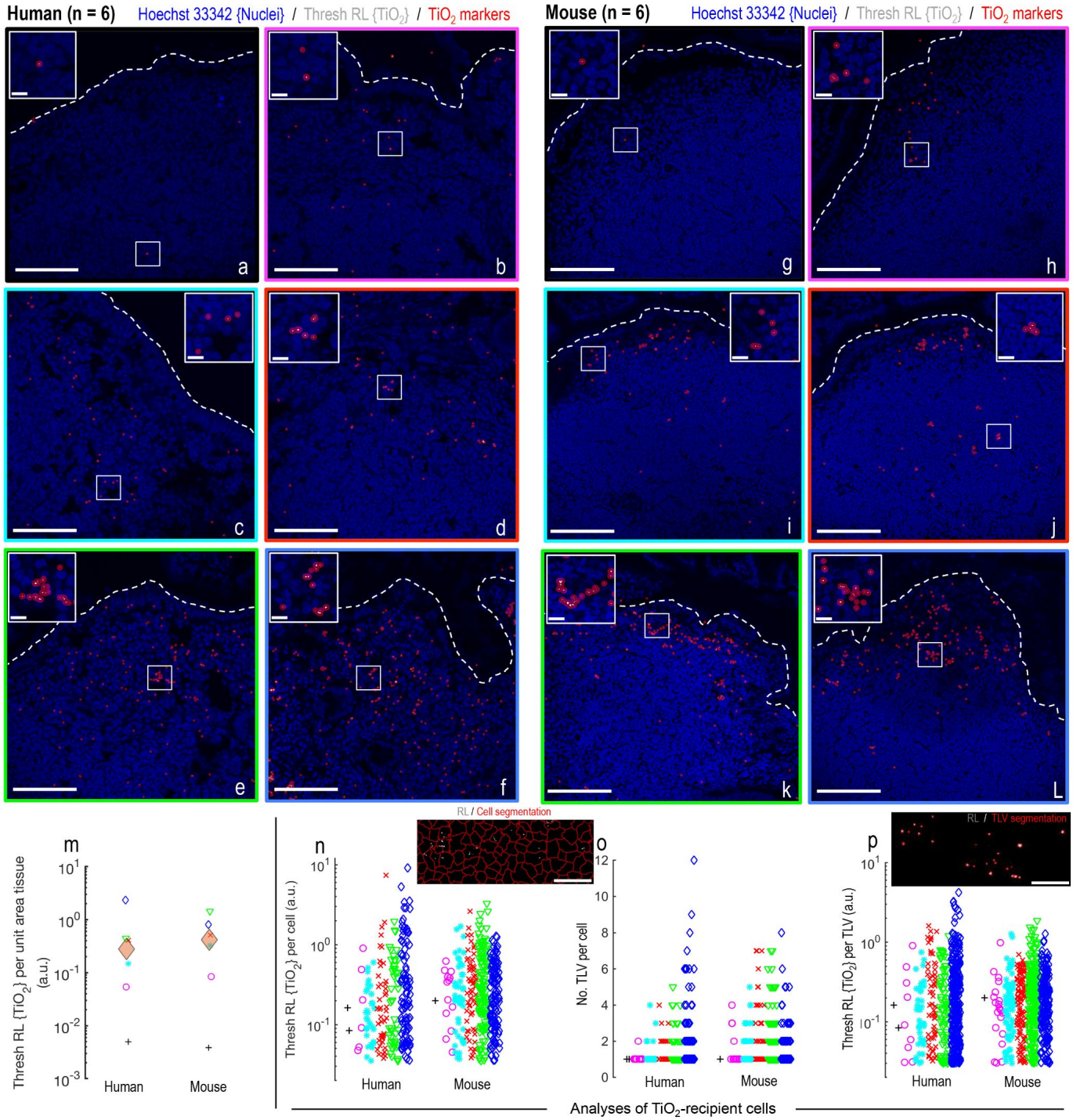

Figure 3 – Establishing correlative human-mouse dosimetry. a-L, Confocal reflectance microscopy showing the range of cellular loading in the subepithelial dome tissue region of (**a-f**), six randomly-drawn human and (**g-L**) six randomly-drawn mouse samples. After acquisition, the image-fields per specimen were manually laid out in order of lowest-to-highest $fgTiO_2$ SED accumulation to visually present the wide variation in $fgTiO_2$ cellular loading. Translucent red circle-markers were placed on thresholded reflectant foci to aid visualisation. **m-p**, Quantitative analysis of the image-data shown in **a-L**. **m**, Thresholded reflectance per unit tissue area (*i.e.,* amount of $fgTiO_2$ per unit tissue area). **n**, Thresholded reflectance per cell (*i.e.,* $fgTiO_2$ dose per cell). **o**, Number of thresholded reflectant foci per cell (*i.e.,* number of $fgTiO_2$-loaded vesicles (TLV) per cell). **p**, Thresholded reflectance signal per foci (*i.e.,* $fgTiO_2$ dose per TLV). Statistical comparison of the distributions is presented in **Supplementary Figure 6** (two-sided Wilcoxon rank-sum analysis). None of the measured $fgTiO_2$ distributions were found to be entirely unique to either species. **m-p**, By all of the quantitative measures established, feeding a murine diet supplemented with 0.0625% (w/w) $fgTiO_2$ for eighteen weeks provides significant overlap with measured, real-world human exposures. *Scale bars:* ***a-L*** *= 50 µm with insets 10 µm;* ***n*** *= 20 µm;* ***p*** *= 5 µm.*

227 **$fgTiO_2$ selectively targets immunocompetant cells.** The $fgTiO_2$-targeted cells in the SED were,
228 unsurprisingly, $CD11c^+$ (*i.e.,* phagocytic mononuclear cells) and not only was the frequency of such
229 cells unaffected by the presence of $fgTiO_2$ particles so was their expression of the CD11c integrin
230 biomarker (**Figure 4a-h**). Neighbouring cells were chiefly $CD3^+$ (T cells) and $B220^+$ (B cells) and,
231 similarly, their expression patterns and frequencies were not significantly affected by the presence of
232 $fgTiO_2$ ($P \geq 0.26$, two-sided unpaired samples T-tests) (**Figure 4a-h**). Within the Peyer's patch,
233 $CD11c^+$ cells are known to exhibit a number of sub-phenotypes in distinct follicular locations[17]. In
234 this regard, the SED localisation and autofluorescence of the $fgTiO_2^+$ cells were entirely consistent
235 with 'LysoMacs' and/or 'LysoDCs' which represent extensively-described macrophage and dendritic
236 cell subsets, respectively, that express high levels of lysozyme alongside a unique autofluorescence
237 signature[17, 23] (see **Figure 4i-s** and **Supplementary Figure 8** for the autofluorescence spectra
238 collected). Indeed, phenotypic markers that help differentiate LysoDCs from LysoMacs (cell surface
239 CD4 and MHCII) demonstrated a mixed population of these two cell types for the $fgTiO_2^+$ cells
240 (**Figure 4t/u**).
241
242 Whilst similar populations of autofluorescent^{hi} SED cells were observed in all mice regardless of
243 diet, these cells were strongly particle-positive in mice receiving the dietary $fgTiO_2$ (**Figure 4m/s,**
244 **Supplementary Figure 9** and **Supplementary Video 1**). Upon quantification (**Figure 4o**), only
245 ~7% of autofluorescent cells showed no clear particle signal for the $+fgTiO_2$ group (**Figure 4i-s**).
246 These cells are known to be important in the initial uptake and processing of luminal antigen which
247 other work suggests may be coated in calcium phosphate to facilitate enzyme resistance during the
248 early phases of the lumen-to-phagocyte sampling process[24]. Except in Crohn's disease, these cells
249 have been shown previously to be positive for the immunoregulatory cell surface ligand PD-L1[25].
250 Again, consistent with this prior work, our quantitative single-cell tissue analyses showed that the
251 $fgTiO_2^+$ (and therefore $CD11c^+$, autofluorescence^{hi}) cells of the SED were PD-$L1^+$ (**Figure 4v-y**,

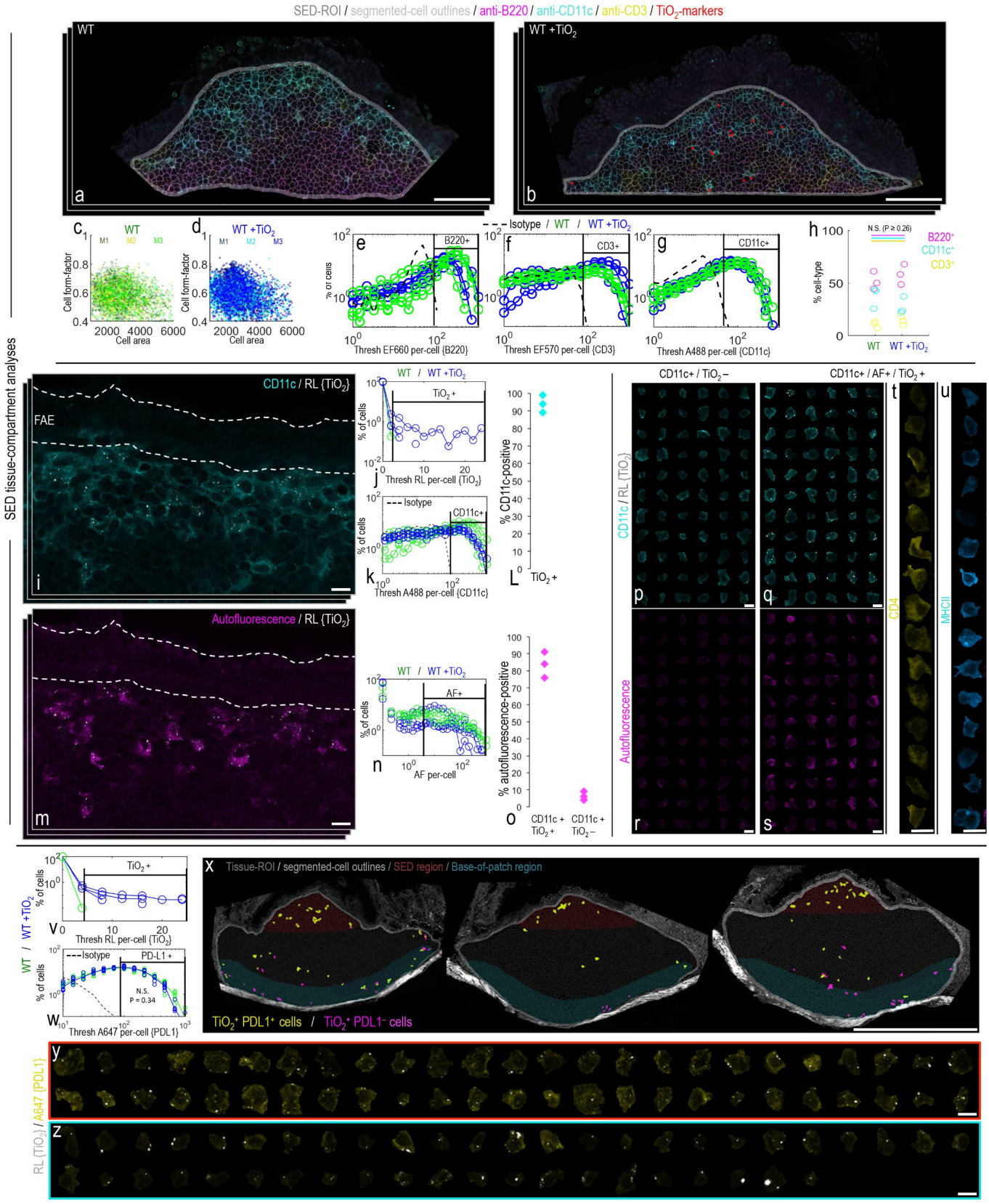

Figure 4 – fgTiO$_2$ selectively targets PD-L1$^+$ LysoMac and LysoDC cells. a-h, *In situ*, single-cell analysis of key immune-cell subtypes of the mouse subepithelial dome. **a/b**, Example images immunofluorescently labelled for B220, CD3 and CD11c (*i.e.,* identifying B-lymphocytes, T-lymphocytes and phagocytic mononuclear cells, respectively) from wild-type (WT) mice fed (**a**) without (WT) or (**b**) with (WT + TiO$_2$) fgTiO$_2$ dietary supplementation (0.0625% w/w of diet). fgTiO$_2$ was measured from thresholded reflectance images. Translucent red circle-markers are placed on reflectant foci to aid visualisation. **c/d**, Flow cytometry-type plots showing cell area / cell aspect ratio, (**e-g**) immunofluorescence distributions and (**h**) cell counts for B220$^+$, CD11c$^+$ and CD3$^+$ cells (n = 3 animals). All measures remained similar regardless of fgTiO$_2$ feeding (cell count comparison (**h**), P = ≥0.26, two-sided unpaired samples T-tests). **i-L**, fgTiO$_2$-recipient cells of the subepithelial dome were CD11c$^+$ in ~ 95% of cases. **m-o**, These cells also exhibited a unique, highly autofluorescent signature as previously-described for subepithelial dome 'lysomac' and 'lysoDC' mononuclear phagocyte cells. **o**, Again, this was true for almost all fgTiO2$^+$/CD11c$^+$ cells and, equally, these autofluorescent cells were similarly present in (**n**) controls without fgTiO$_2$ feeding (further data shown, **Supplementary Figure 8**). **p-u**, Montaged CD11c$^+$/fgTiO$_2^+$ or CD11c$^+$/fgTiO$_2^-$ cell populations from the SEDs of mice fed the fgTiO$_2$ supplemented diet visualised in terms of **(r/s)** autofluorescence signature. fgTiO$_2$ is seen to both selectively and specifically target the autofluorescent cells and (**t/u**) the diversity of CD4 and MHCII expression confirms that both lysomac and lysoDCs take up fgTiO$_2$. **v-z**, fgTiO$_2^+$ cells of the SED expressed the immunotolerance marker programmed death ligand 1 (PD-L1) whereas fgTiO$_2^+$ pigment cells at the base of the Peyer's patch tended to lose PD-L1 expression (**y** versus **z**, respectively). **w**, PD-L1 expression in the Peyer's patches was not significantly perturbed by feeding the fgTiO$_2$-supplemented diet (P = 0.34, z = -0.96, two-sided Wilcoxon rank-sum analysis, n = 6 animals). *Scale bars:* ***a/b*** *= 50 µm;* ***i/m***, ***p-u*** *= 10 µm;* ***x*** *= 500 µm;* ***y/z*** *= 10 µm.*

252 antibody controls presented **Supplementary Figure 10**). This contrasted with precursor pigment
253 cells at the base of the Peyer's patch which were PD-L1^{lo}, despite their fgTiO$_2$ content (**Figure 4v-z**).
254 In other words, based on this finding, and that mice unexposed to fgTiO$_2$ show similar PD-L1$^+$
255 distributions (**Figure 4w)**, we can conclude that expression of this immunoregulatory molecule is
256 unaffected by fgTiO$_2$ uptake ($P = 0.34$, $z = -0.96$, two-sided Wilcoxon rank-sum analysis) and,
257 rather, fgTiO$_2$ is selectively and specifically shuttled into already-PD-L1$^+$ LysoMacs/LysoDCs in the
258 SED of Peyer's patches in the small intestine. As such, for the first time, we show that there *is* an
259 immunocompetent cell population that accumulates fgTiO$_2$ in humans, and in a rodent model, which
260 will now allow the proposed adverse effects of the particulates to be tested.
261
262 **Potential for fgTiO$_2$ – *Salmonella* interactions.** As noted above, in earlier *in vitro* work, we have
263 shown that the phagocyte proinflammatory response can be augmented by cellular loading with
264 fgTiO$_2$[1]. As such "Mouse Study 2" considered the potential for fgTiO$_2$ to initiate or augment an
265 inflammatory response, precisely in the Peyer's patch-rich, terminal ileal region where the particles
266 accumulate. Initiation was measured directly whilst, for augmentation, we investigated the synergy
267 between fgTiO$_2$ and an orally-delivered auxotrophic *Salmonella* strain, namely Δ*aroA*-deficient
268 *Salmonella enterica* serovar Typhimurium (Δ*aroA*-*Salmonella*). The choice of bacterial infection
269 was because (i) again, it is human-relevant (*i.e.,* commonly experienced[26]) (ii) it targets LysoDCs
270 and LysoMacs[27] resulting in a modest immuno-inflammatory response (unlike bacterial fragments, to
271 which the intestine is uniquely tolerant) and (iii) this response can be augmented leaving headroom
272 for any interactions to be observed[28, 29]. Regarding this latter point, it is known that same-cell
273 concurrence of an amplification signal, such as over-expressed bacterial flagellin or co-expressed
274 vectorised cytokines, is required to augment the *Salmonella*-induced immuno-inflammatory
275 response[29, 30]. For this reason, we first demonstrated substantial same-cell occurrence of the particles
276 and bacteria, in the SED of Peyer's patches, when fgTiO$_2$-fed mice (for 16 weeks) were immediately

277 chased with a single oral dose of Δ*aroA*-*Salmonella* and tissues collected 3 days later (+ 3 days;
278 **Figure 5a-c**). *Salmonella*-specific faecal IgA was undetectable at this time-point but was clearly
279 demonstrated in a second group at + 28 days following the *Salmonella* challenge. This pattern was
280 irrespective of $fgTiO_2$ ingestion (**Figure 5d**) and is consistent with a latent immuno-inflammatory
281 response following oral exposure to the pathogen[31, 32].
282
283 To investigate both initiation and augmentation of an inflammatory response, and to cover a broad
284 array of potential outcomes, we undertook protein quantification using the sensitive and accurate
285 (*i.e.,* dual antibodies per target) proximity extension assay (Olink Mouse Exploratory Panel) which
286 provided data for 92 different protein biomarkers (repeat-sample and dilution controls presented,
287 **Supplementary Figure 11**; full protein names shown in **Supplementary Table 1)**. Since
288 *Salmonella* Typhimurium induces a Th1 profile in the ileum[33] we first confirmed, using this
289 analytical approach, that associated cytokines/chemokines were enhanced in ileal tissue from mice
290 that had been challenged with Δ*aroA*-*Salmonella*. Of Th1 relevance, the proximity extension panel
291 detects IL-1 (α&β), TNFα, IL-6, CXCL9 and CCL3[33, 34] and four of these markers (CCL3, CXCL9,
292 IL1β and TNFα) showed significantly ($P \leq 0.026$, two-sided Wilcoxon rank-sum tests) increased
293 protein expression in the ileum of Δ*aroA*-*Salmonella*-exposed mice versus unexposed matched
294 controls at the +28 day time-point (**Figure 5e**). Next we considered the effect on the ileum of chronic
295 oral exposure to $fgTiO_2$ (*i.e.,* mimicking the Peyer's patch loading seen in humans) in the absence of
296 *Salmonella.* The proximity extension assay data showed remarkable consistency between the two
297 groups for all measurable proteins and, therefore, no suggestion that long-term $fgTiO_2$ ingestion
298 initiates inflammatory signalling in the ileum of wild-type mice (**Figure 5f** and **Supplementary**
299 **Figure 12**). In a similar fashion, we considered the effect on the ileum of chronic oral exposure to
300 $fgTiO_2$ plus *Salmonella* infection. Again, not one protein differed significantly in its expression
301 between the groups receiving *Salmonella* and *Salmonella* + $fgTiO_2$ (**Figure 5f** and **Supplementary**

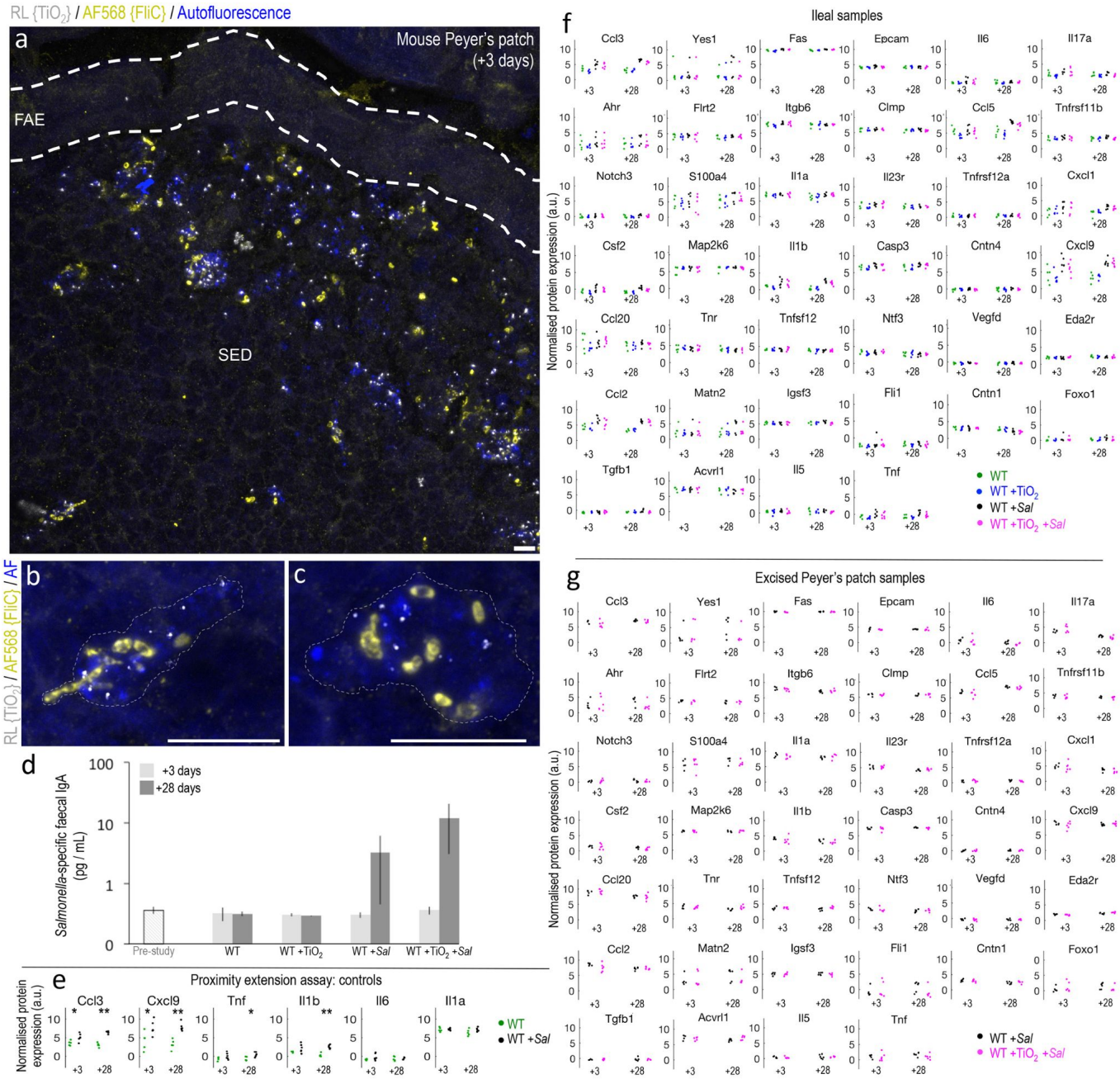

Figure 5 – fgTiO$_2$-*Salmonella* interactions. To enable studies of particle adjuvanticity and cell migration, in "Mouse Study 2", after the 16-week fgTiO$_2$ feeding period all animals were switched to a normal laboratory chow diet (*i.e.,* without fgTiO$_2$-supplementation) then half were orally inoculated with attenuated, Δ*aroA-Salmonella*. Tissues were harvested +3 or +28 days after infection. **a-c**, Confocal reflectance micrographs displayed as z-stack maximum projections showing immunofluorescent labelling for flagellin (FliC) to detect the Δ*aroA-Salmonella* in the Peyer's patch SED region. Marked accumulation of both fgTiO$_2$ and Δ*aroA-Salmonella* was observed in autofluorescent, phagocytic mononuclear cells at the +3 timepoint. **d**, Faecal ELISA studies confirmed a marked, *Salmonella*-specific IgA response at the +28 timepoint (bars represent medians with interquartile range error-bars, n = 3-6 samples per treatment group). **e-g**, Protein expression analyses of ileal tissue digests by proximity extension assay (OLINK mouse exploratory panel). **e,** Comparison of ileal tissues taken from wild-type (WT) mice unexposed to fgTiO$_2$ but with (WT +*Sal*) or without (WT) Δ*aroA-Salmonella* infection confirmed significant increases in expression of key cytokines / chemokines associated with a Th1 immune response ($P \leq 0.026$, two-sided Wilcoxon rank-sum test, n = 5-6 tissues per group). **f**, Inflammation-associated protein expression analyses of ileal tissue digests in the WT, WT +TiO$_2$, WT +*Sal* and WT +TiO$_2$ +*Sal* treatment groups at the +3 and +28-day timepoints. No significant differences were observed between the WT and WT +TiO$_2$ ($P \geq 0.53$, two-sided Wilcoxon rank-sum test, n = 3 animals per group) or WT + *Sal* and WT +TiO$_2$ +*Sal* groups ($P \geq 0.79$, two-sided Wilcoxon rank-sum test, n = 6 animals per group). Full dataset is shown in **Supplementary Figure 12**. **g**, Peyer's patch-focussed inflammation-associated protein expression analyses using carefully-excised patch digests in mice treated with either Δ*aroA-Salmonella* alone (WT +*Sal*) or with fgTiO$_2$ and Δ*aroA-Salmonella* (WT +TiO$_2$ +*Sal*) at +3 or +28 timepoints. No significant differences were observed between the two groups ($P \geq 0.2$, two-sided Wilcoxon rank-sum test, n = 6 animals per group) at either timepoint demonstrating no interaction of fgTiO$_2$ and Δ*aroA-Salmonella* despite (**a-c**) heavy loading into the same cells (full dataset shown in **Supplementary Figure 13**). OLINK protein abbreviations are defined in **Supplementary Table 1**. *Scale bars:* ***a-c*** *= 10 µm.*

302 **Figure 12**) indicating no measurable augmentation of $fgTiO_2$ on *Salmonella*-induced immuno-
303 inflammatory signalling in the ileum of wild type mice, in spite of substantial same-cell uptake of the
304 bacteria and the $fgTiO_2$ particles. To ensure that some small effect, localised to the Peyer's patch as
305 the site of particle accumulation, had not been missed (*e.g.,* 'diluted-out' by surrounding, unaffected
306 tissue) we made the same analyses for a potential augmentation effect using ileal tissue samples that
307 were trimmed tightly to either side of Peyer's patch such that each sample primarily consisted of
308 only the patch itself. But, again, no significant differences in protein expression were measureable by
309 the Olink array (**Figure 5g** and **Supplementary Figure 13**).
310
311 **Cellular dosimetry and ileal tissue distribution.** Finally, we considered what factors influenced
312 $fgTiO_2$ distribution in the Peyer's patch. In the absence of *Salmonella* challenge we observed $fgTiO_2$
313 in autofluorescent cells of the Peyer's patch SED region, as well as some further towards the base of
314 the patch, at both the +3 and +28 day time-points (**Figure 6a/b**), consistent with observations in
315 Mouse Study 1. Quantitatively, however, between the two time points, there was a measurable
316 increase in the number of $fgTiO_2$-loaded vesicles per cell, without a change in load per vesicle, in the
317 mid-region of the follicle (**Figure 6c-j**), suggesting a natural history of vesicular inheritance by
318 certain cells and gradual development towards the well-reported basal pigment cells[15, 16, 20]. Along
319 this pathway, cells maintained the same autofluorescent profile and mixed MHCII and CD4
320 expression as described in Mouse Study 1 suggesting that any such process does not give rise to a
321 new population of cells. Visually however, with increasing distance from the SED, an increase in
322 CD4 expression in conjunction with a decrease in MHCII expression was observed, suggesting an
323 shift to sequestration in cells with the longer-lived, LysoMac phenotype (shown, **Supplementary**
324 **Figure 14)**. A more remarkable influence on the spatial distribution of $fgTiO_2$ was caused by the
325 single oral dose of Δ*aroA*-*Salmonella*. SEDs were almost entirely devoid of $fgTiO_2$ and
326 autofluorescence-positive cells at +28 days (**Figure 6k**), while some cells of the regular villous

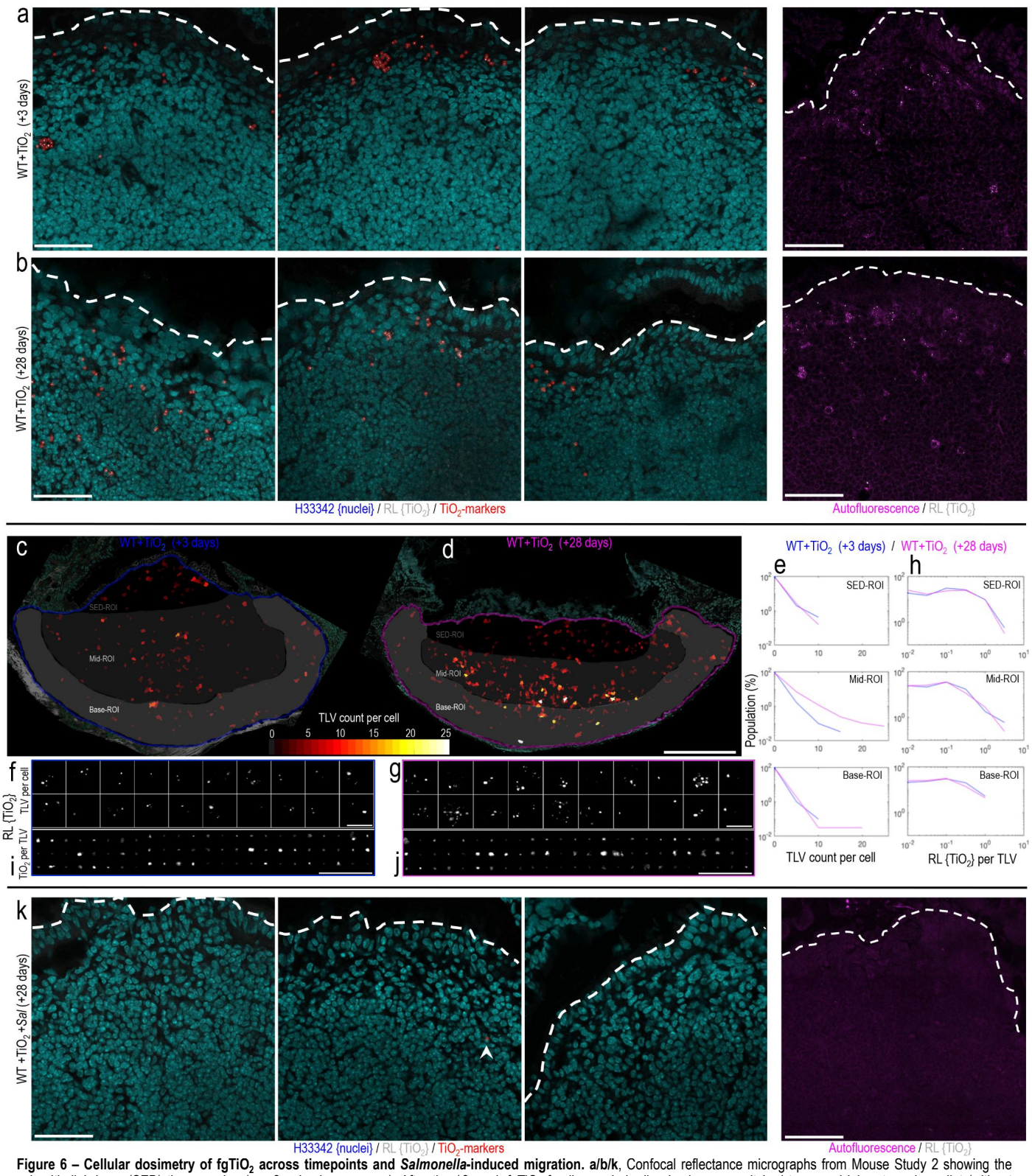

Figure 6 – Cellular dosimetry of fgTiO$_2$ across timepoints and *Salmonella*-induced migration. a/b/k, Confocal reflectance micrographs from Mouse Study 2 showing the subepithelial dome (SED) tissue region (n = 3 animals per group). After the 16-week fgTiO$_2$ feeding period, all animals were switched to normal laboratory chow diet (without fgTiO$_2$ supplementation) and half were orally dosed with Δ*aroA-Salmonella* before tissue harvest at +3 or +28-day timepoints. **a/b**, In the animals fed the fgTiO$_2$-supplemented diet without *Salmonella* exposure (WT +TiO$_2$), fgTiO$_2$-loaded cells were present in the SEDs at both +3 and +28 timepoints. **c-j**, To gain insights into cellular dosimetry changes across the two timepoints, quantitative image analysis of complete Peyer's patch transverse sections was used to precisely measure the number of reflectant foci per-cell (*i.e.,* the fgTiO$_2$-loaded vesicle (TLV) count per-cell) and the amount of reflectance per foci (*i.e.,* equivalent to the fgTiO$_2$ dose per-vesicle). **d/e**, At the +28 timepoint, the TLV count per-cell was markedly elevated with a new population of cells with TLV counts >13 forming in the mid-to-base regions of the follicle. **f/g**, Randomly sampling and montaging the reflectance (RL) information in cells from each of the two timepoints visually demonstrates this, showing (**g**) more heavily-loaded cells at the +28 timepoint. **h**, Moving from cell to vesicle information, in contrast, the amount of reflected light per individual foci remained near-identical across the two timepoints and this was again borne out visually when (**i/j**) individual TLVs were randomly montaged. Collectively, the results suggest that once fgTiO2-loaded cells move below the SED, there is a process of vesicular inheritance by certain cells over time, providing a route to the formation of heavily-loaded pigment cells at the follicle base – as is well-described in humans (**Figure 1**). **k**, Challenge with Δ*aroA-Salmonella* (WT +TiO$_2$ +*Sal*) markedly changed this picture (n = 4 animals per group). At the +28 timepoint, SEDs were almost completely devoid of both fgTiO$_2$ and autofluorescence-positive cells. Out of four SEDs imaged, only one reflectant foci was detectable (indicated by arrow) showing marked migration of fgTiO$_2$ from the SED tissue compartment after Δ*aroA-Salmonella* exposure. *Scale bars:* ***a/b/k*** *= 50 µm,* ***c/d*** *= 250 µm,* ***f/g/i/j****, = 10 µm.*

327 lamina propria, as well as of the basal aspect of the Peyer's patch, were now positive for $fgTiO_2$
328 (**Figure 7a-c**; enlarged display with counterstaining context, **Supplementary Figure 15**).
329 Consistently, it has been reported that oral danger signals, including *Salmonella*, deplete the Peyer's
330 patch SED region of prior-absorbed plastic microparticles[35]. The pathway that then enables
331 appearance of $fgTiO_2$ in sporadic cells of the regular mucosa, as we show here, is not clear but (i)
332 $fgTiO_2$ loading per cell was low versus most Peyer's patch cells (**Figure 7b/c**) and (ii) many of these
333 cells showed an autofluorescent signature (**Figure 7d**). As such, LysoDC migration from the patch
334 with re-homing to the gut mucosa should be considered.
335
336 **DISCUSSION**
337 In this work, we have exploited the growing accessibility of machine learning methods[36] to enable
338 precise analyses of complex images yielding *in situ* single-cell and single-vesicle data from tissue
339 samples with full locational data retained. Particle selectivity of cellular targets in distinct tissue
340 regions can thus be assessed[37, 38]. Access to quantitative single-cell and vesicle measurements has
341 provided an unprecedented opportunity to compare and establish cell-dose equivalence between
342 humans and mice. The findings move the field forward in four important areas of persistent particle
343 exposure via the oral route, namely: (i) human relevance (ii) mechanism of absorption and intestinal
344 distribution (iii) role in intestinal inflammation and (iv) provision of a model for cogent risk
345 assessment.
346
347 **Human relevance.** The human small intestine is the only known site of cellular accumulation of
348 dietary microparticles, as exemplified by $fgTiO_2$[16, 18, 20] (**Figure 1**). We show here that all features of
349 this can be qualitatively and quantitatively recapitulated in a murine model, but full achieving this
350 requires exposure to human-relevant microbial 'danger signals'. Consistently, in this work, murine
351 dosing with $fgTiO_2$ was undertaken in a manner that reflects real-life exposures (*i.e.,* via the diet at

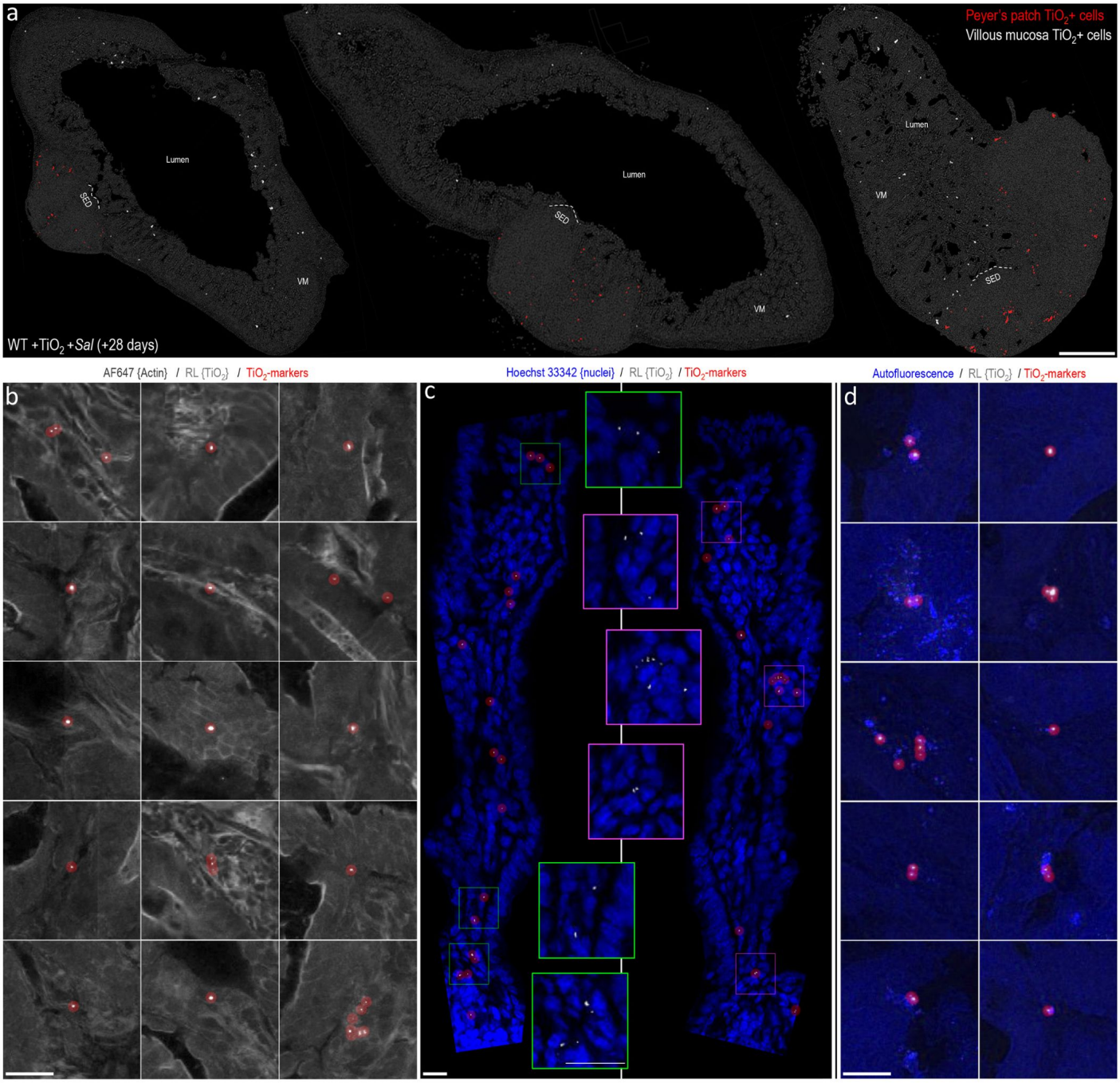

Figure 7 – Ileal distribution of fgTiO$_2$ following *Salmonella* challenge. a, Single-cell image analysis of tilescanned confocal reflectance images collected from transverse sections of mouse ileal tissue from the fgTiO$_2$-exposed, Δ*aroA-Salmonella*-infected treatment group (+28-day timepoint, n = 3 animals). fgTiO$_2$-positive cells in the Peyer's patches are displayed in red. As in **Figure 6**, the subepithelial dome (SED) regions were devoid of fgTiO$_2$ with the majority of the positive cells located basally around the follicle margins. In contrast to all previous data collected without Δ*aroA-Salmonella* exposure, fgTiO$_2$-positive cells (displayed in white) were now also present in the villous mucosa. Bigger versions of the single-cell analyses presented in (**a**) are available in **Supplementary Figure 15**. **b**, Montaging positive events from villous mucosa regions showed that particle loading was low compared to Peyer's patch cells with the majority containing single reflectant foci. **c**, High resolution imaging of optically cross-sectioned villi confirmed reflectant foci deep in the lamina propria in the same manner as observed in humans (**Figure 1c**). **d**, The majority of the fgTiO$_2$-positive events in the villous mucosa also displayed the same autofluorescence signature as was observed in the particle-recipient cells of the SED. *Scale bars:* ***a*** *= 250 µm;* ***b-d*** *= 20 µm.*

352 relatively low levels for a long period of time). Our findings contrast with a prior study, which used
353 bolus dosing via oral gavage or surgical intervention in fasted animals, where direct $fgTiO_2$ uptake
354 via the epithelium was reported[39]. Future work may wish to consider the necessity of natural
355 ingestion and concomitant normal microbial exposures, versus non-physiological dosing in specific
356 pathogen free environments, to recapitulate the human situation and address risk accurately for oral
357 particle exposures.
358
359 **Mechanism of absorption and intestinal distribution.** Seminal early work from Frey and Mantis[40,
360 41] showed that the mucus-rich glycocalyx markedly impairs model particle uptake by the regular
361 villous epithelium, whereas the near-absence of these features overlying Peyer's patches allows
362 direct access of particulates to M-cells. These cells have an extraordinary ability to engulf luminal
363 particles and macromolecules, passing them through to abutting cells at their basolateral membrane.
364 We first confirmed, unequivocally, that this uptake mechanism holds true for $fgTiO_2$ and, next,
365 demonstrated that specific SED immuno-competent phagocytes (LysoMacs and LysoDCs) are the
366 direct recipient cells that accumulate cargo from the M-cell. Taking all of our data together, we
367 believe that there is an on-going process of slow re-arrangement, typified by vesicular inheritance by
368 some of the cells and gradual particle-loaded-cell movement to the base of the patch. This migration
369 (presumed to occur in LysoMacs), which must ultimately result in mature pigment cell formation[16,
370 18], is greatly accelerated by oral exposure to the bacterial pathogen *S.* Typhimurium. In addition,
371 some particulate migration out of the patch, to the villous lamina propria, also occurs (typically low-
372 loaded cells, presumed LysoDCs). Again, building on formative work on the fate of reporter particles
373 of fluorescent plastic in the Peyer's patch[35], it is likely that the 'danger signal effect' holds true for
374 oral exposure to soluble enterotoxin adjuvants as well as pathogenic bacteria (*i.e.* multiple human-
375 relevant danger signals). Continuous exposure to $fgTiO_2$, as happens for many human populations,
376 would then re-load the apical (SED) phagocytes until another danger signal event occurs. Thus, for

377 the first time, we describe the natural history of persistent particle routing through – and beyond –
378 the Peyer's patch following oral exposure. This explains basal pigment cell accumulation of multiple
379 particle types, including titanium dioxide, silica and aluminosilicates, in human Peyer's patches as
380 well as the occurrence of sporadic particles elsewhere in cells of the small intestine[16, 18, 20].
381
382 **Role in intestinal pathology.** By extension of the above observations, our findings also imply that
383 $fgTiO_2$ is not in itself perceived as a danger signal in the intestine of wild-type mice since a
384 secondary (microbial) signal is still required for the 'acute' migration. Moreover, using highly
385 sensitive and selective protein analyses, that captured a broad array of biomarkers of immuno-
386 inflammatory signalling, we were unable to identify either direct or augmented perturbation of tissue
387 homeostasis at the site of particle accumulation. Indeed, mammals have very likely evolved with oral
388 exposure to other fine particles (*e.g.,* geologically-derived and soot). Certainly aluminosilicates, in
389 abundance, and some forms of silica are reported in human Peyer's patches alongside titanium
390 dioxide[16, 18]. Perhaps therefore, effective compensatory mechanisms generally exist, which may
391 include constitutive cell expression of immuno-inhibitory PD-L1 (**Figure 4v-z**).
392
393 Notwithstanding, the potential for $fgTiO_2$- induction or augmentation of intestinal pathology still
394 deserves scrutiny. First, in subjects with Crohn's disease, fine-particle-targeted macrophages of the
395 Peyer's patch do *not* express PD-L1[25]. Interestingly, Crohn's disease is a relatively modern
396 inflammatory disorder and there is good evidence that it may initiate in the Peyer's patches[42]. The
397 most commonly-associated single gene mutation with the disease is NOD2 and there is *in vitro*
398 evidence that when NOD2 is perturbed $fgTiO_2$ augments enhanced inflammatory activity with
399 microbial fragments[1]. So it should now be carefully considered what impact the ingestion of $fgTiO_2$
400 has on at-risk genotypes and, especially, where NOD2 functionality is diminished or removed.
401 Secondly, it is important to note that conclusions from this work refer to the distal small intestine

402 where there is uptake of $fgTiO_2$. As noted previously[12], however, it does not shed light on potential
403 effects of $fgTiO_2$ where it is *not* absorbed such as in the large intestine. Direct luminal effects (on
404 microbiome or apical enterocytes for example) cannot be precluded, especially given that this is
405 where exposure will be by far the greatest. Indeed, both Urrutia-Ortega *et al.,*[43] and Bettini *et al.,*[44]
406 have provided evidence for direct, pro-tumorigenic effects of $fgTiO_2$ on the colon which deserves
407 further attention[12].
408
409 **A model for cogent risk assessment.** Finally, we note that the particulate-accumulating population
410 of apical SED cells are clearly (i) immunocompetent (*i.e.,* non-quiescent) based upon their migration
411 characteristics, expression of cell surface immunoregulatory PD-L1 and their previously-described
412 qualities in terms of antimicrobial defence[17, 27, 45, 46] and (ii) capable of becoming heavily loaded with
413 $fgTiO_2$. Indeed, the exquisite particle selectivity for this tissue region means that the concentration
414 gradient for area-corrected reflectance signal was ~14-fold higher than for the Peyer's patch overall
415 and, therefore, ~1,245 fold higher than that of villous mucosa (**Supplementary Figure 16**). Given
416 that the particulate-loaded phagocytic cells make up only a minority of the SED[17, 23], then the cell
417 concentration of $fgTiO_2$ is *very* high (**Supplementary Video 1**).
418
419 We know of no other active particle-funnelling and specific cell-targeting strategy elsewhere in
420 mammalian biology so it is very likely that SED LysoMacs and LysoDCs provide the first and only
421 target to enable highly sensitive, single-cell risk assessment of $fgTiO_2$ and other persistent oral
422 particulates *in vivo*. By exemplification, we addressed the question of whether $fgTiO_2$ could initiate
423 or augment inflammatory signaling in the ileum / Peyer's patches of wild type mice: a long standing
424 question in the field. The clear answer was 'no', at least in wild-type genotypes, despite some *in*
425 *vitro* evidence to the contrary[1]. To explain such differences it is worth noting that cell culture studies
426 fail to replicate *in vivo* fidelity in many ways including rates of particle uptake, presence of

427 functional lymphatics and vasculature, cellular cross-talk, compensatory mechanisms and cell
428 migration prior to particle saturation (cell gorging). Whatever the reasons, after decades of
429 uncertainty, other questions regarding the safety of persistent oral particles can now be precisely
430 addressed using *in vivo* studies with human-relevant dosimetry and identified target cells. Indeed,
431 understanding the consequences of LysoMac / LysoDC accumulation of persistent particles in terms
432 of genotoxicity and any differential responses resultant from distinct host genotypes is now key to
433 understanding human risk following oral exposure to nanoparticles and microparticles.
434

435 **METHODS**

436 **Mouse Study 1**

437 The first mouse $fgTiO_2$ feeding study was approved by the Grasslands Animal Ethics Committee
438 (Palmerston North, New Zealand) in accordance with the New Zealand Animal Welfare Act 1999.
439 Food-grade, anatase TiO_2 particles ($fgTiO_2$) were purchased from Sensient Colors (St. Louis, MO,
440 USA). Physico-chemical characterisation of these particles in our previous work shows a particle
441 diameter distribution of ~ 50 – 300 nm, with a median diameter of ~ 130 nm[1]. As described and
442 extensively characterised previously[15], to enable successful oral delivery, the standard rodent diet
443 American Institute of Nutrition (AIN)-76A was supplemented with 0.000625%, 0.00625% or
444 0.0625% (w/w) $fgTiO_2$ (translating to approximately 1, 10 or 100 mg $fgTiO_2$ / kg body-weight / day
445 respectively[15]). These diets were prepared by Research Diets (New Brunswick, NJ, USA), with
446 straight AIN-76A without $fgTiO_2$ supplementation used as the 'negative control diet'. Six-week-old
447 mice (C57BL/6, 50:50 male:female) were housed conventionally with normal feed intake and
448 weight-gain confirmed bi-weekly[15]. After eighteen weeks feeding, mice were euthanised by CO_2
449 asphyxiation and cervical dislocation. The gastrointestinal tract was quickly removed and placed in
450 cold phosphate-buffered saline (PBS). Ileal tissues containing the most distal Peyer's patches (*i.e.,*
451 closest to the ileal/caecal junction) and adjacent caecal patches were excised and frozen on a cold,
452 stainless steel bar embedded in dry ice. Tissues were then transferred into cryomolds filled with pre-
453 cooled optimal cutting temperature compound (OCT) and transferred to – 80°C for storage.

454

455 **Mouse Study 2**

456 Animal experiments conducted at Cambridge were performed under the authority of Home Office
457 personal license number PIL IEDB62633, and project license number PPL PF86EABB1. Female
458 mice (C57BL/6) were purchased from Charles River Laboratories (UK). Upon arrival, mice were
459 housed conventionally and were monitored for signs of normal health, food ingestion and body-

460 weight gain throughout the study period. At the start of the study, thirty-six mice (six weeks old)
461 were randomly divided into two feeding groups. As before, one group received the standard rodent
462 diet American Institute of Nutrition (AIN)-76A supplemented with 0.0625% (w/w) $fgTiO_2$
463 (translating to approximately 100 mg $fgTiO_2$ / kg body-weight / day respectively[15]) whereas the
464 other received straight AIN-76A without $fgTiO_2$ supplementation (*i.e.,* the negative control diet).
465 After sixteen weeks of feeding, all mice were switched to the negative control diet, and twelve mice
466 from each diet-group were orally challenged with Δ*aroA*-deficient, *S.* Typhimurium strain SL3261[47]
467 (Δ*aroA*-*Salmonella)*. We marginally separated the administrations of bacteria and $fgTiO_2$ to (i)
468 prevent artefactual adsorption due to co-administration (ii) enable luminal interactions between
469 gavaged bacteria and residual luminal particles (demonstrated by faecal ICP-MS studies,
470 **Supplementary Figure 17**) should such interactions occur and (iii) ensure that some food also was
471 in the lumen under these circumstances as would be expected with normal feeding. Mice were lightly
472 anaesthetised with isofluorane then orally gavaged with 0.2 mL of inoculum prepared at 5.25×10^9
473 CFU/mL. Mice were then euthanised by CO_2 asphyxiation and cervical dislocation at two time-
474 points, either +3 or +28 days after *Salmonella* inoculation (*i.e.,* 16 weeks +3 days or 16 weeks +28
475 days). In this way, four treatment groups (n = 6 control diet, n = 12 control diet + *Salmonella*, n = 6
476 $fgTiO_2$ diet, n = 12 $fgTiO_2$ diet + *Salmonella*) were established, with half of the animals analysed at
477 each of the two time-points. Alongside, faecal samples were collected at three time-points (pre-
478 study, 16 weeks +3 days and 16 weeks +28 days) to enable enzyme-linked immunosorbent assay
479 (ELISA) studies for *Salmonella*-specific IgA and faecal Ti measurements by ICP-MS.
480
481 **Human tissue collection**
482 Following informed consent, and after approval from the Regional Ethical Review Board,
483 Linköping, Sweden, surgical specimens containing Peyer's patches were collected from the neo-
484 terminal ileum from six patients with Crohn's disease or colonic cancer (3 males, 3 females;

resection date-range 2017-2018; median age 48 years; age-range 21 – 77 years). In all instances the ileal tissue specimens formed the resection margins and were macroscopically normal. Peyer's patches were microscopically identified as previously described[48]. The tissue specimens were fixed with 4% PBS-buffered (pH 7.4) paraformaldehyde for 12 h at 4°C before immersion in 30% sucrose and freezing in OCT (LAMB/OCT, Thermo Scientific) in cryomolds. For analysis, the OCT-embedded tissue samples were rapidly shipped overnight to Cambridge on dry ice. Three anonymised, formalin-fixed paraffin embedded (FFPE) tissue samples containing ileal Peyer's patch lymphoid tissue were also analysed to confirm the presence of $fgTiO_2$ in the FFPE specimen-type. Studies using human tissues at Cambridge were also approved by the UK NHS Health Research Authority, North West – Greater Manchester East Research Ethics Committee, REC reference 18/NW/0690.

Tissue sectioning and immunofluorescence labeling

Frozen sections were cut at 20-micron thickness using a Leica CM 1900 cryostat, picked up on Superfrost Plus slides (ThermoFisher, J1800AMNT) and rested at room temperature for 2 h prior to labelling. FFPE sections were cut at 5-micron thickness, then dewaxed and rehydrated by baking at 60°C for 1 h, transferring through two changes of xylene, a reverse ethanol series (100%, 70%, 50%, 10%) followed by 1 minute rehydration in water. Sections were ringed with hydrophobic barrier pen (Vector Laboratories, H-4000) and cryostat sections fixed by exposure to fresh 4%, 0.1M PBS-buffered paraformaldehyde (pH 7.4) for 10 min. All subsequent steps were conducted under gentle agitation on a rotating shaker. To facilitate antibody penetration, sections were permeabilised for 90 min using 0.3 % (vol/vol) Triton X-100 in 0.1 M PBS (pH 7.4). Block buffer (10% goat serum, 2% bovine serum albumin, 25 mM glycine diluted in 25 mM Tris-buffered (pH 7.4) saline (TBS)) was then added to all sections for 1 hour. Primary antibodies or concentration-matched isotype controls were diluted in block-buffer and incubated at 4°C overnight. All subsequent steps took place at room

510 temperature. Sections were washed with three changes of block-buffer. Secondary antibodies (where
511 directly-conjugated primary antibodies were not used) were diluted 1:400 in block buffer and
512 incubated for 2 h. All antibody concentrations, fluorophore conjugations and manufacturer
513 information are provided in **Supplementary Table 2**. 500 nM phalloidin-AlexaFluor 647
514 (ThermoFisher, A22287) and 2 µg/mL Hoechst 33342 (ThermoFisher, H3570) were also included
515 alongside secondary antibodies to simultaneously label cell outlines (*i.e.,* cytoskeletal f-actin) and
516 cell nuclei (respectively). Sections were then washed once with TBS prior to mounting with #1.5
517 coverslips in Prolong Diamond (ThermoFisher, P36965).
518
519 **Confocal microscopy & imaging controls**
520 Fluorescence and reflectance image-data (2048x2048 pixels per tile) were collected using a diode-
521 controlled (retrofitted) Zeiss LSM780 confocal microscope equipped with plan-apochromat 63X/1.4
522 and 40X/1.3 oil-immersion objectives. Fluorescence and reflectance data were collected at the same
523 time during the same imaging run by sequential scanning with reflected (*i.e.,* back-scattered) light
524 from a 488 nm excitation laser collected in the range 485 – 491 nm to detect $fgTiO_2$[15]. Where
525 tilescanning was used, images were acquired with 10% edge overlap. Tiles were stitched using the
526 Zen Black 2011 SP2 software (Carl-Zeiss, UK) using the nuclei and actin channels for registration
527 and a 'strict' correlation threshold setting of 1.0. For all datasets under comparison, images were
528 obtained in a single run using identical settings. For the reflectance imaging, tissues from negative
529 control mice (*i.e.,* fed the AIN-76 diet only, so no $fgTiO_2$ present) were used to determine the image
530 acquisition settings and thresholding for $fgTiO_2$ detection (strategy shown, **Supplementary Figure**
531 **1**). For immunofluorescence work, supporting secondary-only and concentration-matched isotype
532 antibody controls in tissue-matched serial sections were included. For datasets collected as sets of
533 single images from the villous mucosa (VM), sub-epithelial dome (SED), germinal center (GC) and
534 TCZ (T-cell zone) regions of mouse Peyer's patches, landmarks (*e.g.,* villi / follicle-associated

535 epithelium) and T cell (CD3), B cell (B220) and mononuclear phagocyte (CD11c)
536 immunofluorescence staining in adjacent sections were used to inform imaging locations. When
537 tilescanning was performed, images were collected with 10% edge-overlap using focus mapping to
538 facilitate accurate image stitching whilst minimising acquisition time. To define the autofluorescence
539 signature of the fgTiO_2-recipient cells in the mouse Peyer's patches, lambda scans were performed
540 using the LSM 780 microscope. Using unstained tissue sections, autofluorescence upon excitation
541 from a 405 nm laser was detected in ~ 10 nm intervals in the range 415-700 nm (spectra presented,
542 **Supplementary Figure 8**).
543
544 **Deconvolution**
545 Z-stacked image-data (pixel size (XYZ) 1024x1024x123; voxel size (XYZ) 26x26x100 nm) of
546 fgTiO_2-recipient cells was collected using a Zeiss LSM 780 confocal microscope equipped with a
547 63X/1.4 plan-apochromat oil immersion objective using murine tissue sections embedded in Prolong
548 Glass (P36984, ThermoFisher) anti-fade reagent (refractive index ~ 1.5). Cell autofluorescence was
549 excited using the 405 nm laser. The image-stacks were registered to correct spatial drift using
550 StackReg[49]. The Born and Wolf scalar-based diffraction model[50] was then used to estimate a
551 theoretical point spread function assuming a refractive index of 1.51 and a autofluorescence emission
552 maximum of 495 nm (measured, **Supplementary Figure 8**). The registered Z-stack was then
553 deconvolved using the Richardson-Lucy total variation algorithm (75 iterations, regularisation 1e-12)
554 within the open-source DeconvolutionLab2[51] software.
555
556 **fgTiO_2 detection using reflected light and circle-marker placement**
557 To enable fgTiO_2 detection in biological tissue sections, reflected light and immunofluorescence
558 information was collected at the same time using a Zeiss LSM780 confocal microscope. The
559 reflectance images were thresholded to isolate the punctate, reflectant foci caused by the fgTiO_2

560 particles from the background light scatter caused by the biological tissue. As the background level
561 was similar in both mouse and human specimens (shown, **Supplementary Figure 4**) the same
562 threshold was used for both mouse and human images, and was determined as the level required to
563 remove all signal in the reflectance channel for images collected for tissue sections taken from the
564 negative control mice (*i.e.,* fed the AIN-76 diet only, so no $fgTiO_2$ present). This approach was then
565 further validated using correlative scanning electron microscopy and energy dispersive X-ray
566 analyses to confirm that the signal remaining after thresholding contained the expected X-ray signal
567 for titanium (strategy shown, **Supplementary Figure 1**). Given the small size of the reflectant foci
568 caused by $fgTiO_2$, a translucent circle-marker was placed on each pixel above the threshold using the
569 'insertShape' function in MATLAB R2021a (MathWorks) to aid visualisation given the relatively
570 small size of display in the Figure panels[15]. Examples of the raw signal and subsequent marker
571 placements are shown for mouse and humans in **Supplementary Figure 5**. Example data and code
572 demonstrating thresholding and circle marker placement are available at the BioStudies database
573 under accession number S-BSST875.
574
575 **Correlative confocal-electron microscopy and energy dispersive X-ray analyses**
576 Once $fgTiO_2$ detection by confocal reflectance microscopy was completed, Prolong-mounted
577 coverslips were removed from the tissue sections by overnight incubation in PBS at 37°C. Slides
578 were air dried at room temperature for 24 h, cut down and mounted on aluminum SEM stubs using
579 colloidal graphite and coated with a thin (~ 15 nm) layer of amorphous carbon (evaporative coater).
580 Tissue sections were then loaded into a Helios G4 CX Dual Beam high-resolution, monochromated,
581 field emission gun, scanning electron microscope (SEM) equipped with a precise focused ion beam
582 (FIB) and in-lens secondary electron and circular backscattered detectors (FEI/ThermoFisher).
583 Secondary and backscattered electron images were collected at 3 – 5 kV as tilescans for the complete
584 tissue surface, permitting manual overlay onto the previously-collected confocal tilescans. To enable

585 correlative confocal-SEM imaging, the 'outline' of the Peyer's patch – particularly the follicle
586 associated epithelium and basal muscularis layer – were manually registered together using image
587 overlay, enabling triangulation to target specific regions containing reflectance-positive cells. The
588 correlative confocal-to-EDX analyses of the human tissues were then carried out directly in the
589 SEM, using a 150 mm^2 silicon drift detector and AZTEC software (Oxford Instruments). For the
590 correlative scanning transmission electron microscopy (STEM) used to confirm single-particle
591 detection by reflectance microscopy, thin lamella of the tissue sample were prepared in the SEM via
592 the *in situ* lift-out method. Once sites-of-interest had been identified, 500 nm of electron beam
593 platinum (Pt) was deposited (at 5 kV, 6.4 nA for the electron source) to the surface of the target area.
594 This was followed by a second Pt layer (1 μm) using the FIB (at 30 kV, 80 pA for the liquid
595 gallium (Ga) ion source). A bulk lamella was initially cut using the FIB (at 30 kV, 9 nA), before the
596 final cut-out was performed (at 30 kV, 80 pA). The lamella was attached, using ion beam Pt, to a
597 copper FIB lift-out grid (Omniprobe, USA) mounted within the SEM chamber (*i.e., in situ*). Final
598 thinning and polishing of the lamella to electron translucency was performed with a gentle
599 polish/clean using the ion beam (5 kV, 41 pA). A lamella was then transferred into a Titan^3 Themis
600 G2 300 kV S/TEM equipped with an S-TWIN objective lens, monochromator, HAADF detector and
601 a Super-X 4-detector EDX system in a double-tilt specimen holder (FEI/ThermoFisher).
602 Transmission electron microscopy (TEM) images and on-zone diffraction patterns were recorded
603 using a OneView CMOS camera (Gatan) and STEM-EDX elemental maps were recorded and
604 processed using the Velox software (FEI/ThermoFisher).
605
606 **Cell segmentation of intestinal tissue images**
607 In previous work, we carefully developed and validated staining and image analysis methods
608 enabling extraction of single-cell data from confocal microscopy images of gastrointestinal tissues[37].
609 Based on this framework, three cell segmentation pipelines were used to accommodate different

610 tissue types and differing availabilities of training data. To confirm the reliability of our previously-
611 published pipelines with the new image-data presented here, the accuracy of the outputs from all
612 three cell segmentation pipelines were assessed relative to manually-segmented cells by Jaccard
613 index (presented, **Supplementary Figure 2)**.
614
615 **Cell segmentation: mouse villous mucosa images**
616 Villous image-fields were directly segmented into cell-objects using the freely-available CellProfiler
617 software[52]. Using the Hoechst 33342 fluorescence information, nuclei were first segmented as
618 primary objects. These were then used as seeds during a marker-controlled watershed process to
619 segment each cell's outline using fluorescence information from the actin channel. The process is
620 schematically demonstrated in **Supplementary Figure 18** with the complete CellProfiler pipeline
621 shown in **Supplementary Note 1**. Test images and the CellProfiler pipeline are also available for
622 download at the BioStudies database under accession number S-BSST875.
623
624 **Cell segmentation: mouse lymphoid tissue images**
625 Lymphoid tissues (*e.g.,* Peyer's patches and caecal patches) exhibit extremely high cell densities
626 leading to poor cell segmentation accuracies using the simple, marker-controlled watershed approach
627 used for the villous mucosa images[37]. Pixel-classification machine learning can be used to alleviate
628 this problem through the generation of probability images that more precisely delineate each cell's
629 boundary[37]. Here, in mouse lymphoid tissues, these probability images were provided using a 2-D U-
630 Net fully convolutional neural network[53] deployed in MATLAB R2021a (MathWorks, MA). The
631 network has a 256x256x2 (x, y, channels) input layer and uses the nuclear and actin fluorescence
632 information to predict the probability that each pixel belongs to either 'cell outline', 'intracellular
633 environment' or 'background' classifications. The training data consisted of twelve lymphoid tissues
634 images (each containing 2138 x 1900 annotated pixels covering ~16,000 cells prepared by an

635 experienced cell biologist). The image-data flows through a four-layer contracting convolutional
636 path before complete up-convolutional expansion, yielding probability images that exactly match the
637 input-image dimensions. The network was trained for 50 epochs using a batch-size of 12 for 1,200
638 iterations/epoch. Patches were shuffled every epoch and augmented by simple, random x / y
639 reflection and rotation. Model training was optimised under stochastic gradient descent using cross-
640 entropy loss. The initial learning rate was 0.05, dropping every 10 epochs by 0.1 under momentum
641 0.9 and L2 regularisation $1x10^{-4}$. The resultant 'Cell Outline' probability images were then loaded
642 into the CellProfiler pipeline alongside immunofluorescence and reflectance information collected
643 by the confocal microscope and were used to enable segmentation of individual cells via an
644 'IdentifyPrimaryObjects module'. This process is schematically demonstrated in **Supplementary**
645 **Figure 19.** The complete CellProfiler image analysis pipeline is presented in **Supplementary Note**
646 **2**. All U-Net code, the trained network with test-data and the complete CellProfiler pipeline are
647 available for download from the BioStudies database under accession number S-BSST875.
648
649 **Cell / TLV segmentation: correlative mouse-human dosimetry**
650 For the correlative analyses investigating the relative amounts of $fgTiO_2$ delivered to individual SED
651 cells in mice versus in normally-exposed humans, frozen ileal tissue sections containing Peyer's
652 patches were collected at random from six normally-exposed humans, and six mice fed the AIN-67
653 diet supplemented with 0.0625% (w/w) $fgTiO_2$. In every instance, care was taken to collect tissue
654 sections with clear follicle-associated epithelium (*i.e.,* without any overlying villi) to ensure
655 maintenance of similar histological positioning near the 'center of the dome' of each Peyer's patch.
656 Reflectance confocal images of the murine and human tissues were then acquired in a single run
657 under identical settings. After acquisition, the image-fields per specimen were manually laid out in
658 order of lowest-to-highest $fgTiO_2$ accumulation to visually present the spectrum of (wide) variation
659 in $fgTiO_2$ cellular loading observed across samples in both the mouse and human tissue specimens.

660 This was followed by quantitative image analysis to determine the thresholded reflectance per unit
661 tissue area; then the integrated intensity of the threshold reflectance information per-cell and per-
662 vesicle objects (method exemplified, **Supplementary Figure 3**). To extract the single-cell and
663 single-vesicle data, a CellProfiler pipeline was used. To tackle cell segmentation in lymphoid tissues
664 with high cell densities we have shown in previous work[37] that pixel-classification machine learning
665 can be used to produce probability images that more precisely delineate each cell's boundary
666 improving segmentation accuracies when compared to using the raw fluorescence information.
667 Unlike in mouse lymphoid tissues (method described above), because large amounts of manually-
668 annotated training data for the human lymphoid images was not available, these probability images
669 were created by sparse annotation pixel-classification machine learning in the ILASTIK software[54].
670 Two ILASTIK pixel-classification projects were created (one for the human images, one for the
671 mouse). Pixel annotations representing 'intracellular environment', 'cell outlines' and 'other'
672 classifications were made on the fluorescence channel describing the cell outlines (*i.e.,* the actin
673 channel) (method shown schematically, **Supplementary Figure 20**). The ILASTIK software then
674 generated probability images representing the probability of each pixel belonging to each
675 classification. The resultant 'Cell Outline' probability images were loaded into the CellProfiler
676 pipeline alongside the fluorescence and reflectance information captured by the confocal microscope
677 and were used to segment individual cells via an 'IdentifyPrimaryObjects' module. As part of this
678 pipeline, the reflectant foci representing $fgTiO_2$ events were also directly-segmented from the
679 thresholded reflectance images into '$fgTiO_2$-loaded vesicle' (TLV) objects using a second,
680 'IdentifyPrimaryObjects' module (method schematically demonstrated, **Supplementary Figure 21**).
681 The complete image analysis pipeline is presented in **Supplementary Note 3**. Test images and the
682 complete CellProfiler pipeline are available for download from the BioStudies database under
683 accession number S-BSST875. The accuracy of the segmented-cell outputs were checked by Jaccard
684 index relative to manually-segmented cells (presented, **Supplementary Figure 2)**. The accuracy of

685 TLV segmentation from the raw reflectance information is explored in both mouse and human
686 images in **Supplementary Figure 5.**
687
688 **Cell / TLV feature extraction**
689 As described in previous work[37], raw immunofluorescence data were pre-processed by manual
690 thresholding at the level required to remove ≥ 95% of fluorescence in tissue-matched, secondary
691 antibody-only control images. Alongside, the reflectance data were carefully thresholded at the level
692 required to remove all signal from the images collected from the negative control group mice (*e.g.,*
693 fed the AIN-67 diet alone; strategy shown, **Supplementary Figure 1**). Thresholded reflectance and
694 fluorescence intensity information per cell or TLV object, alongside size and shape features were
695 then measured for both the immunofluorescence and reflectance channels using the
696 'MeasureObjectSizeShape' and 'MeasureObjectIntensity' modules in CellProfiler. The number of
697 TLV objects per cell was measured using a 'RelateObjects' module. Data were preprocessed by
698 discarding objects outside of the 5th and 95th percentiles by size prior to analysis as is recommended
699 best-practice[55].
700
701 **Cell segmentation: block processing tilescans**
702 To avoid memory limitations, when necessary, tilescanned images were cut into smaller pieces, run
703 through one of the CellProfiler pipelines before reassembling the object segmentation masks and
704 assigning global cell position coordinates to the extracted object features. This was achieved using
705 two MATLAB functions developed in our previous work[37]. The first 'TilescanToCellProfiler', reads
706 stitched images in most microscopy formats and cuts them into manageable tiles with edge-overlap
707 for processing. The second, 'CellProfilerToTilescan' reassembles the object masks, removes 'double
708 hits' on overlap edges and assigns global position coordinates values to the extracted features.

709 Example images and MATLAB code demonstrating these functions is available for download at the
710 BioStudies database under accession number S-BSST875.
711
712 **Cell segmentation: accuracy assessment by Jaccard index**
713 The Jaccard index (intersection over union) approach was used to check the accuracy of the cell
714 segmentation results used in this work. This was achieved by comparing pixel positions inside the
715 automatically-segmented cell objects against those obtained by manual annotations performed by an
716 experience cell biologist. The Jaccard index was calculated as:
717
718 $$J(A,M) = \frac{|A \cap M|}{|A \cup M|} = \frac{|A \cap M|}{|A| + |M| - |A \cap M|} \qquad \text{(Equation 1)}$$
719
720 Where J is the Jaccard distance for two sets of pixel positions for the automated (A) and manual (M)
721 segmentations, respectively. Scores of zero represent no overlap (false negatives) whereas scores of
722 1 represent exact pixel-for-pixel intersection. In this way, it is acknowledged that this approach is a
723 relatively harsh success measure, and that scores of ~ 0.7 indicate a good segmentation result[53]. This
724 is partially due to the inevitable inaccuracies that are present – even in the manually-annotated data
725 (*e.g.,* due to outline smoothing, ambiguity in determining the precise position of each cell's boundary
726 from the fluorescent staining information, and the available image resolution *etc.*).
727
728 **Cell segmentation: cell mapping visualisations**
729 The cell map visualisations displaying the delivered cellular doses of $fgTiO_2$ or TLV counts per-cell
730 were produced using cell feature information extracted by the CellProfiler
731 'MeasureObjectIntensities' and 'RelateObjects' modules alongside the object segmentation masks
732 outputted by each pipeline. Using MATLAB scripts, object feature data were binned into categories
733 (*e.g.,* 'low, 'intermediate' and 'high' $fgTiO_2$-load based on the integrated intensity of the thresholded

734 reflectance signal per-cell). Using the segmentation masks, individual cell-objects were then colour-
735 coded according to these categories to provide a 'tissue map' visualisation. Example data and
736 MATLAB code demonstrating the creation of these visualisations are available for download from
737 the BioStudies database under accession number S-BSST875.
738
739 **Statistical analysis of image-based data**
740 Integrated intensity per object (*i.e.,* per cell or NLV) distributions were compared using two-sided
741 Wilcoxon rank-sum analysis. This non-parametric approach was chosen for compatibility with
742 unpaired samples with unequal group sizes[37]. The approach tests the null hypothesis that the
743 distributions under comparison might reasonably be drawn from one continuous distribution with
744 equal medians ($P > 0.05$) versus the alternate hypothesis that the distributions are distinct ($P \leq 0.05$).
745 Pairwise comparisons of cell counts were first checked for distribution normality and variance
746 homogeneity using Shapiro-Wilk and Barlett tests, respectively. Where these tests were passed (P
747 >0.05), groups were compared using a two-sided, unpaired samples T-test assuming equal variance.
748
749 **Olink® proximity extension assay**
750 Frozen mouse ileal samples were weighed and stored in Kimble pellet pestle tubes (DWK Life
751 Sciences, K-749520-0000) at -70°C until processing. The Peyer's patch-enriched samples were first
752 trimmed tightly to either side of Peyer's patch using a cold safety razorblade such that each sample
753 primarily consisted of only the patch itself. Tissues were lysed using the BioPlex Cell Lysis Kit
754 (BioRad, 171-304011). 500 µL of Cell Wash Buffer per sample was used for rinsing the tissues. Cell
755 Lysis Buffer was prepared by adding Factors 1 and 2 as per the manufacturer's instructions, as well
756 as Halt Protease Inhibitor Cocktail (ThermoFisher, 78437; 10 µL of cocktail per 1 mL of buffer).
757 Following a rinse, tissues were homogenised by adding 500 µL of ice-cold Cell Lysis Buffer and
758 hand grinding on ice using disposable pestles (DWK Life Sciences, 749520-0000; 20 strokes).

759 Homogenised samples were frozen at -70°C for at least 4 hours, thawed on ice, sonicated in an
760 Ultrawave U300 ultrasonic bath (44 kHz, 35 W) on ice for 40 seconds and centrifuged for 5 min at
761 6,000 x g. Supernatant was collected into 2 mL cryogenic vials (Corning, 430659) and frozen at -
762 70°C until quantification. Quantification was performed using the DC Protein Quantification Kit I
763 (BioRad, 5000111) as per the manufacturer's instructions (Microplate Assay Protocol). Plates
764 (Greiner Bio-One, 650185) were read using FLUOstar Omega microplate reader at 750 nm and
765 protein concentrations were calculated by the Omega's MARS Data Analysis software using linear
766 regression fit. All samples were normalised to 0.77 mg/mL (+/- 0.12) by dilution with Cell Lysis
767 Buffer and re-quantified to confirm protein concentration. A microplate was prepared for the
768 proximity extension assay by transferring 40 µL aliquots of all samples, negative controls (Cell Lysis
769 Buffer), duplicates of 6 samples, and dilutions (1:4, 1:8 and 1:16 v/v) of two samples into a 96-well
770 skirted plate (ThermoFisher, AB0800) in a randomised manner (controls presented, **Supplementary**
771 **Figure 11**). The plate was sealed (ThermoFisher, 4306311) and stored at -70°C until shipment on
772 dry ice to Olink (Uppsala, Sweden) for analysis using the Target 96 Mouse Exploratory panel
773 (www.olink.com/mouse-exploratory). All protein names and abbreviations are listed in
774 **Supplementary Table 1**. Statistical analysis was performed using the Olink Analyze 3.6.0 R-
775 package (https://CRAN.R-project.org/package=OlinkAnalyze). Treatment groups were compared
776 using a two-sample Mann-Whitney U test with correction for multiple testing using the Benjamini-
777 Hochberg method. In the main text, results for proteins that could be involved in immuno-
778 inflammatory signaling are shown (**Figure 5**) whereas in the Supplementary Information results of
779 the entire protein set are shown alongside repeat-sample, serial dilution and blank sample proximity
780 extension assay controls (**Supplementary Figures 11-13**). The proximity extension assay data are
781 available for download at the BioStudies database under accession number S-BSST875.
782
783 **Enzyme-linked immunosorbent assay for *Salmonella*-specific IgA**

784 During Mouse Study 2, faecal pellets were collected pre-study and at the 16-week +3 day and 16-
785 week +28 day time-points. Samples were weighed and diluted 1:10 (w/v) in 10% PBS containing 1
786 mM EDTA. The resulting suspension was vortexed for 15 min to facilitate liquefaction then
787 centrifuged at 400 x g at 4°C for 5 min. The supernatant was aspirated and centrifuged for a second
788 time at 12,000 x g for 10 min at 4°C. *Salmonella*-specific IgA quantification was then carried by
789 sandwich ELISA method. Plates were coated with 50 µL lipopolysaccharide (LPS), (Sigma, L2262)
790 diluted in Reggiardo's buffer (0.05 M glycine, 0.1 M NaCl, 1 mM EDTA, 0.05 M NaF and 0.1%
791 sodium deoxycholate). Plates were then sealed and incubated overnight at 37°C. Next day, the plates
792 were washed 3 times with PBS-tween and blotted dry. Blocking buffer from the whole IgA kit
793 (Affymetrix, 88-50450) was added to each well for 1 hr at 37°C. The faecal supernatant was then
794 diluted in kit buffer A (Affymetrix, 88-50450) and 50 µL of diluted sample was added to each well.
795 After three hours of incubation, the plates were washed three times with PBS-tween before addition
796 of 50 µL horseradish peroxidase-conjugated IgA. Three more washes were carried out before the
797 addition of 50 µL tetramethylbenzidine substrate for 10 min. This was followed by 50 µL of stop
798 solution prior to absorption reading at 492 nm on a plate reader. All outputs were calibrated using a
799 standard curve and corrected for dilution.
800
801 **Faecal ICP-MS analysis**
802 Faecal samples were collected and stored at -80°C. Samples were weighed and a digestion solution
803 of 1:1 (vol/vol) nitric acid (Fisher, 7697-37-2) and hydrogen peroxide (Sigma, 7722-84-1) was added
804 to the samples (20-70 mg faecal weight) at a 1:10 (wt/vol) ratio. Samples were digested at room
805 temperature for 72 h before loosely-capped sample containers were transferred to a water bath
806 (40°C) for 5-6 h to release the peroxide. Samples were then transferred to a PTFE vial and sulphuric
807 acid was added (1:1 vol acid/sample weight) prior to final digestion using a Milestone UltraWave
808 microwave. The resultant liquid was decanted and diluted 1:10 (vol/vol) using ultra-high purity

water. Quantification of elemental Ti was performed using an 8900 triple quadruple inductively-coupled plasma mass spectrometer (Agilent, USA). Scans were performed in MS/MS mode with the reaction cell adjusted for analysis in H_2/O_2 gas. The instrument was set up to identify the mass pairs 48 and 64 for isotopic Ti-48 and TiO_2-64. Calibration standards were prepared in 2% nitric acid and spiked with elemental Ti (Sigma, 12237) to final concentrations between 0 and 1 ppm. All samples were spiked with an internal standard solution containing gallium (Sigma, 16639), germanium (Sigma, 05419), yttrium (Sigma, 01357) & europium (Sigma, 05779) at final concentrations of 2 ppb. Counts per-second (cps) values for yttrium were collected to reference signal stability. A 2% solution of nitric acid was used as sample carrier and rinse.

ONLINE CONTENT

Data and code are available at the BioStudies database (https://www.ebi.ac.uk/biostudies/) under accession number S-BSST875.

DATA AVAILABILITY

Data supporting the presented analyses are available for download from the BioStudies database (https://www.ebi.ac.uk/biostudies/) under accession number S-BSST875. Source data are provided with this submission.

CODE AVAILABILITY

MATLAB code (using Deep Learning, Image Processing and Computer Vision toolboxes) and CellProfiler pipelines enabling the presented image analysis workflows are downloadable from the BioStudies database (http://www.ebi.ac.uk/biostudies) under accession number S-BSST875.

834 **REFERENCES**

835

836 1. Riedle S, Pele LC, Otter DE, Hewitt RE, Singh H, Roy NC*, et al.* Pro-inflammatory adjuvant
837 properties of pigment-grade titanium dioxide particles are augmented by a genotype that
838 potentiates interleukin 1β processing. *Part. Fibre Toxicol.* 2017, 14(1): 51.

839

840 2. Ashwood P, Thompson RP, Powell JJ. Fine particles that adsorb lipopolysaccharide via bridging
841 calcium cations may mimic bacterial pathogenicity towards cells. *Exp. Biol. Med.* 2007, 232(1):
842 107-117.

843

844 3. Grand View Research. Titanium dioxide market size, share and trends analysis report by grade
845 (anatase, rutile), by production process (sulfate, chloride), by application (paints and coatings,
846 plastics), by region, and segment forecasts, 2021 - 2028.
847 https://www.grandviewresearch.com/industry-analysis/titanium-dioxide-industry - accessed
848 December 3rd, 2022.

849

850 4. Safety assessment of titanium dioxide (E171) as a food additive. *EFSA J.* 2021, 19(5): e06585.

851

852 5. European Medicines Agency. Final feedback from European Medicines Agency (EMA) to the
853 EU Commission request to evaluate the impact of the removal of titanium dioxide from the list of
854 authorised food additives on medicinal products.
855 https://www.ema.europa.eu/en/documents/report/final-feedback-european-medicine-agency-ema-
856 eu-commission-request-evaluate-impact-removal-titanium_en.pdf - accessed December 3rd,
857 2022.

858

6. Bekiempis V. Taste the toxin? Skittles 'unfit for human consumption', lawsuit claims. https://www.theguardian.com/business/2022/jul/15/skittles-mars-lawsuit-titanium-dioxide-toxin - accessed December 3rd, 2022.

7. Food Standards Australia and New Zealand. Review of titanium dioxide as a food additive. https://www.foodstandards.gov.au/consumer/foodtech/Pages/Review-of-titanium-dioxide-as-a-food-additive.aspx - accessed December 3rd, 2022.

8. Committee on Toxicity of Chemicals in Food, Consumer Products and the Environment. Interim position paper on titanium dioxide. https://cot.food.gov.uk/sites/default/files/2022-01/TiO2%20COT%20Interim%20position%20paper.pdf - accessed December 3rd, 2022.

9. Health Canada. Titanium dioxide (TiO2) as a food additive: current science report. https://www.canada.ca/en/health-canada/services/food-nutrition/reports-publications/titanium-dioxide-food-additive-science-report.html - accessed December 3rd, 2022.

10. Hewitt RE, Chappell HF, Powell JJ. Small and dangerous? Potential toxicity mechanisms of common exposure particles and nanoparticles. *Curr. Opin. Toxicol.* 2020, 19: 93-98.

11. Kirkland D, Aardema MJ, Battersby RV, Beevers C, Burnett K, Burzlaff A*, et al.* A weight of evidence review of the genotoxicity of titanium dioxide (TiO_2). *Regul. Toxicol. Pharmacol.* 2022, 136: 105263.

12. da Silva AB, Miniter M, Thom W, Hewitt RE, Wills J, Jugdaohsingh R*, et al.* Gastrointestinal absorption and toxicity of nanoparticles and microparticles: myth, reality and pitfalls explored through titanium dioxide. *Curr. Opin. Toxicol.* 2020, 19: 112-120.

13. Heringa MB, Peters RJB, Bleys R, van der Lee MK, Tromp PC, van Kesteren PCE*, et al.* Detection of titanium particles in human liver and spleen and possible health implications. *Part. Fibre Toxicol.* 2018, 15(1): 15.

14. Kreyling WG, Holzwarth U, Schleh C, Kozempel J, Wenk A, Haberl N*, et al.* Quantitative biokinetics of titanium dioxide nanoparticles after oral application in rats: Part 2. *Nanotoxicology* 2017, 11(4): 443-453.

15. Riedle S, Wills JW, Miniter M, Otter DE, Singh H, Brown AP*, et al.* A murine oral-exposure model for nano- and micro-particulates: demonstrating human relevance with food-grade titanium dioxide. *Small* 2020, 16(21): e2000486.

16. Powell JJ, Ainley CC, Harvey RS, Mason IM, Kendall MD, Sankey EA*, et al.* Characterisation of inorganic microparticles in pigment cells of human gut associated lymphoid tissue. *Gut* 1996, 38(3): 390-395.

17. Bonnardel J, Da Silva C, Henri S, Tamoutounour S, Chasson L, Montañana-Sanchis F*, et al.* Innate and adaptive immune functions of peyer's patch monocyte-derived cells. *Cell Rep.* 2015, 11(5): 770-784.

906 18. Powell JJ, Faria N, Thomas-McKay E, Pele LC. Origin and fate of dietary nanoparticles and
907 microparticles in the gastrointestinal tract. *J. Autoimmun.* 2010, 34(3): J226-233.
908
909 19. Baranska A, Shawket A, Jouve M, Baratin M, Malosse C, Voluzan O*, et al.* Unveiling skin
910 macrophage dynamics explains both tattoo persistence and strenuous removal. *J. Exp. Med.*
911 2018, 215(4): 1115-1133.
912
913 20. Shepherd NA, Crocker PR, Smith AP, Levison DA. Exogenous pigment in Peyer's patches. *Hum.*
914 *Pathol.* 1987, 18(1): 50-54.
915
916 21. Kimura S, Yamakami-Kimura M, Obata Y, Hase K, Kitamura H, Ohno H*, et al.* Visualization of
917 the entire differentiation process of murine M cells: suppression of their maturation in cecal
918 patches. *Mucosal Immunol.* 2015, 8(3): 650-660.
919
920 22. Donaldson DS, Else KJ, Mabbott NA. The gut-associated lymphoid tissues in the small intestine,
921 not the large intestine, play a major role in oral prion disease pathogenesis. *J. Virol.* 2015,
922 89(18): 9532-9547.
923
924 23. Wagner C, Bonnardel J, Da Silva C, Martens L, Gorvel JP, Lelouard H. Some news from the
925 unknown soldier, the Peyer's patch macrophage. *Cell. Immunol.* 2018, 330: 159-167.
926
927 24. Powell JJ, Thomas-McKay E, Thoree V, Robertson J, Hewitt RE, Skepper JN*, et al.* An
928 endogenous nanomineral chaperones luminal antigen and peptidoglycan to intestinal immune
929 cells. *Nat. Nanotechnol.* 2015, 10(4): 361-369.
930

931 25. Robertson J, Haas CT, Pele LC, Monie TP, Charalambos C, Parkes M, *et al.* Intestinal APCs of
932 the endogenous nanomineral pathway fail to express PD-L1 in Crohn's disease. *Sci. Rep.* 2016, 6:
933 26747.
934
935 26. Centers for Disease Control and Prevention. *Salmonella* and food.
936 https://www.cdc.gov/foodsafety/communication/salmonella-food.html – accessed March 30th
937 2024.
938
939 27. Da Silva C, Wagner C, Bonnardel J, Gorvel JP, Lelouard H. The Peyer's patch mononuclear
940 phagocyte system at steady state and during infection. *Front. Immunol.* 2017, 8:1254.
941
942 28. Hur J, Lee JH. Enhancement of immune responses by an attenuated Salmonella enterica serovar
943 Typhimurium strain secreting an Escherichia coli heat-labile enterotoxin B subunit protein as an
944 adjuvant for a live Salmonella vaccine candidate. *CVI.* 2011, 18(2): 203-209.
945
946 29. Eom JS, Seok Kim J, Im Jang J, Kim BH, Young Yoo S, Hyeon Choi J, *et al.* Enhancement of
947 host immune responses by oral vaccination to Salmonella enterica serovar Typhimurium
948 harboring both FliC and FljB flagella. *PloS ONE.* 2013, 8(9): e74850.
949
950 30. Agorio C, Schreiber F, Sheppard M, Mastroeni P, Fernandez M, Martinez MA, *et al.* Live
951 attenuated Salmonella as a vector for oral cytokine gene therapy in melanoma. *J. Genet. Med.*
952 2007, 9(5): 416-423.
953
954 31. al-Ramadi BK, Meissler JJ, Jr., Huang D, Eisenstein TK. Immunosuppression induced by nitric
955 oxide and its inhibition by interleukin-4. *Eur. J. Immunol.* 1992, 22(9): 2249-2254.

956

957 32. al-Ramadi BK, Chen YW, Meissler JJ, Jr., Eisenstein TK. Immunosuppression induced by
958 attenuated Salmonella. Reversal by IL-4. *J. Immunol.* 1991, 147(6): 1954-1961.
959

960 33. Klimpel GR, Asuncion M, Haithcoat J, Niesel DW. Cholera toxin and *Salmonella* Typhimurium
961 induce different cytokine profiles in the gastrointestinal tract. *Infect. Immun.* 1995, 63(3): 1134-
962 1137.
963

964 34. Fallahi P, Ferrari SM, Ragusa F, Ruffilli I, Elia G, Paparo SR*, et al.* Th1 chemokines in
965 autoimmune endocrine disorders. *J. Clin. Endocrinol. Metab.* 2020, 105(4):1046-1060.
966

967 35. Shreedhar VK, Kelsall BL, Neutra MR. Cholera toxin induces migration of dendritic cells from
968 the subepithelial dome region to T- and B-cell areas of Peyer's patches. *Infect. Immun.* 2003,
969 71(1):504-509.
970

971 36. Strack R. Deep learning in imaging. *Nat. Methods* 2019, 16(1): 17-17.
972

973 37. Wills JW, Robertson J, Summers HD, Miniter M, Barnes C, Hewitt RE*, et al.* Image-Based Cell
974 Profiling Enables Quantitative Tissue Microscopy in Gastroenterology. *Cytometry A.* 2020,
975 97(12):1222-1237.
976

977 38. Rees P, Wills JW, Brown MR, Barnes CM, Summers HD. The origin of heterogeneous
978 nanoparticle uptake by cells. *Nat. Commun.* 2019, 10(1): 2341.
979

980 39. Coméra C, Cartier C, Gaultier E, Catrice O, Panouille Q, El Hamdi S*, et al.* Jejunal villus
981 absorption and paracellular tight junction permeability are major routes for early intestinal uptake
982 of food-grade TiO2 particles: an in vivo and ex vivo study in mice. *Part. Fibre Toxicol.* 2020,
983 17(1):26.
984
985 40. Mantis NJ, Frey A, Neutra MR. Accessibility of glycolipid and oligosaccharide epitopes on
986 rabbit villus and follicle-associated epithelium. *Am. J. Physiol. Gastrointest. Liver Physiol.* 2000,
987 278(6): G915-G923.
988
989 41. Frey A, Giannasca KT, Weltzin R, Giannasca PJ, Reggio H, Lencer WI*, et al.* Role of the
990 glycocalyx in regulating access of microparticles to apical plasma membranes of intestinal
991 epithelial cells: implications for microbial attachment and oral vaccine targeting. *J. Exp. Med.*
992 1996, 184(3):1045-1059.
993
994 42. Keita AV, Söderholm JD. Barrier dysfunction and bacterial uptake in the follicle-associated
995 epithelium of ileal Crohn's disease. *Ann. N. Y. Acad. Sci.* 2012, 1258: 125-134.
996
997 43. Urrutia-Ortega IM, Garduño-Balderas LG, Delgado-Buenrostro NL, Freyre-Fonseca V, Flores-
998 Flores JO, González-Robles A*, et al.* Food-grade titanium dioxide exposure exacerbates tumor
999 formation in colitis associated cancer model. *Food Chem. Toxicol.* 2016, 93: 20-31.
1000
1001 44. Bettini S, Boutet-Robinet E, Cartier C, Coméra C, Gaultier E, Dupuy J*, et al.* Food-grade TiO2
1002 impairs intestinal and systemic immune homeostasis, initiates preneoplastic lesions and promotes
1003 aberrant crypt development in the rat colon. *Sci. Rep.* 2017, 7: 40373.
1004

1005 45. Lelouard H, Henri S, De Bovis B, Mugnier B, Chollat-Namy A, Malissen B*, et al.* Pathogenic
1006 bacteria and dead cells are internalized by a unique subset of Peyer's patch dendritic cells that
1007 express lysozyme. *Gastroenterology* 2010, 138(1): 173-184.
1008
1009 46. Lelouard H, Fallet M, de Bovis B, Méresse S, Gorvel JP. Peyer's patch dendritic cells sample
1010 antigens by extending dendrites through M cell-specific transcellular pores. *Gastroenterology*
1011 2012, 142(3):592-601.
1012
1013 47. Hoiseth SK, Stocker BA. Aromatic-dependent Salmonella typhimurium are non-virulent and
1014 effective as live vaccines. *Nature* 1981, 291(5812):238-239.
1015
1016 48. Keita AV, Gullberg E, Ericson AC, Salim SY, Wallon C, Kald A*, et al.* Characterization of
1017 antigen and bacterial transport in the follicle-associated epithelium of human ileum. *Lab. Invest.*
1018 2006, 86(5): 504-516.
1019
1020 49. Thévenaz P, Ruttimann UE, Unser M. A pyramid approach to subpixel registration based on
1021 intensity. *IEEE Trans. Image Process.* 1998, 7(1):27-41.
1022
1023 50. Kirshner H, Aguet F, Sage D, Unser M. 3-D PSF fitting for fluorescence microscopy:
1024 implementation and localization application. *J. Microsc.* 2013, 249(1):13-25.
1025
1026 51. Sage D, Donati L, Soulez F, Fortun D, Schmit G, Seitz A*, et al.* DeconvolutionLab2: An open-
1027 source software for deconvolution microscopy. *Methods* 2017, 115:28-41.
1028

1029 52. Carpenter AE, Jones TR, Lamprecht MR, Clarke C, Kang IH, Friman O*, et al.* CellProfiler:
1030 image analysis software for identifying and quantifying cell phenotypes. *Genome Biol.* 2006,
1031 7(10):R100.
1032
1033 53. Falk T, Mai D, Bensch R, Çiçek Ö, Abdulkadir A, Marrakchi Y*, et al.* U-Net: deep learning for
1034 cell counting, detection, and morphometry. *Nat. Methods* 2019, 16(1):67-70.
1035
1036 54. Sommer C, Straehle C, Köthe U, Hamprecht FA. Ilastik: Interactive learning and segmentation
1037 toolkit. 2011 IEEE International Symposium on Biomedical Imaging: From Nano to Macro.
1038 2011, 230-233.
1039
1040 55. Caicedo JC, Cooper S, Heigwer F, Warchal S, Qiu P, Molnar C*, et al.* Data-analysis strategies for
1041 image-based cell profiling. *Nat. Methods* 2017, 14: 849-863.
1042

1043 **FIGURE LEGENDS**

1044 **Figure 1 – Titanium dioxide in human intestinal tissues. a**, Tilescanned image acquired by
1045 confocal reflectance microscopy. Reflectant foci were detected along the follicle base consistent with
1046 previously-reported mineral particle-containing "pigment cells". Of note, similar reflectant foci were
1047 also present apically in the immuno-active, subepithelial dome tissue-region, and away from the
1048 patch in the (**c**) lamina propria of the regular villous mucosa (VM). Translucent red circle-markers
1049 are placed on the reflectant foci to aid visualisation. **b**/**d**/**e**, Correlative SEM/EDX analyses
1050 performed on the same tissue section shown in (**a**/**c**). The pigment cell region is shown in (**b**) where
1051 X-ray signal for both Al (attributable to aluminosilicates) and Ti (attributable to titanium dioxide)
1052 was found. EDX analyses in the (**d**) villous mucosa and (**e**) subepithelial dome regions showed
1053 reflectant foci were attributable to Ti. **b**/**d**/**e**, In all instances the elemental data for Ti were a near-

1054 exact match for the reflectant foci, whereas (**b**) areas with Al signal alone did not reflect. **f**,
1055 Reflectance microscopical analyses of nine, randomly-drawn human samples (six frozen, three
1056 formalin-fixed paraffin embedded (FFPE)) showed reflectant foci consistent with TiO_2 in the
1057 subepithelial dome of *every* sample. *Scale bars:* ***a*** *= 50 µm;* ***b*** *= 50 µm with 10 µm insets;* ***c-e*** *= 10*
1058 *µm;* ***f*** *= 50 µm with 10 µm insets.*
1059
1060 **Figure 2 – A mouse feeding study demonstrates $fgTiO_2$ specificity for Peyer's patches. a,** Single-
1061 cell image analysis of a transverse mouse ileal tissue section imaged by tilescanning confocal
1062 reflectance microscopy. The cellular dose of $fgTiO_2$ – measured from the thresholded reflectance
1063 (RL) signal – is colour-coded at low (lo), intermediate (int) and high (hi) levels. As in humans
1064 (**Figure 1a/f**), $fgTiO_2$ loaded into the subepithelial dome of the Peyer's patch and there was evidence
1065 of 'precursor pigment cell' formation along the follicle base. Away from the Peyer's patch, two
1066 positive cells (**a**, insets) were found in the overlying villous mucosa. In contrast to the human
1067 findings (**Figure 1c**) however, both were caused by luminal $fgTiO_2$ trapped in the invaginated space
1068 of goblet cells. **b-d**, To investigate the sensitivity of $fgTiO_2$ detection by confocal reflectance
1069 microscopy, a tissue-region containing a single, isolated reflectant foci was milled out under
1070 correlative SEM using a focussed ion beam (**b/c** shows the registered SEM images transparently
1071 overlaid onto the confocal reflectance data before lift-out. The white 'rectangle' in (**c**) is caused by
1072 electron charging of the platinum strap laid down on the tissue region to be lifted out; (**d**) shows a
1073 side-view of the lifted-out lamella). **e-i**, Transfer of the lamella to a transmission electron microscope
1074 enabled high resolution imaging and X-ray (EDX) and electron diffraction analysis. A (**g/h**) single
1075 particle of $fgTiO_2$ with an (**i**) anatase diffraction pattern (*i.e.,* as added to the diet) was confirmed
1076 responsible for the single reflectant foci observed. **j**, Again, colour-coding the cellular dose of $fgTiO_2$
1077 into lo, int and hi levels, tissue sections from adjacent caecal patches at the top of the colon were
1078 found to be almost completely devoid of $fgTiO_2$ (n = 4 animals). **k**, Immunofluorescence microscopy

1079 showed $fgTiO_2$ access to Peyer's patches was via GP2-positive microfold (M) cells (translucent red
1080 circle-markers are placed on thresholded reflectant foci to aid $fgTiO_2$ visualisation / the outline of the
1081 M-cell was manually drawn by tracing the actin-delineated cell boundary). **L**, Single-cell analysis of
1082 a longitudinal section of mouse ileum consistently showed the close association between an M-cell
1083 rich, follicle-associated epithelium and $fgTiO_2$ loading into Peyer's patches. **m/n**, Guided by CD11c
1084 and CD3 immunofluorescence labelling for phagocytic mononuclear cells and T-lymphocytes
1085 (respectively) sets of images were collected from the subepithelial dome (SED), germinal centre
1086 (GC) T-cell zone (TCZ) or overlying villous mucosa (VM) tissue regions from four mice fed the
1087 $fgTiO_2$-supplemented diet (WT + TiO_2) and four control-diet mice (WT). Some $fgTiO_2$ signal was
1088 observed in the GC and TCZ regions of the murine Peyer's patches but the majority was in the SED.
1089 In keeping with (**a**), and in contrast to the human findings (**Figure 1c**), in all four mice, no uptake
1090 was seen in the villous mucosa demonstrating specificity for M-cell mediated, Peyer's patch
1091 targeting. *Scale bars:* ***a*** *= 500 μm with insets 5 μm;* ***b*** *= 50 μm;* ***c*** *= 10 μm;* ***d*** *= 5 μm;* ***e*** *= 500 nm;* ***g***
1092 *= 200 nm;* ***h*** *= 20 nm;* ***j*** *= 500 μm;* ***k*** *= 10 μm;* ***L/m*** *= 500 μm.*
1093
1094 **Figure 3 – Establishing correlative human-mouse dosimetry. a-L**, Confocal reflectance
1095 microscopy showing the range of cellular loading in the subepithelial dome tissue region of (**a-f**), six
1096 randomly-drawn human and (**g-L**) six randomly-drawn mouse samples. After acquisition, the image-
1097 fields per specimen were manually laid out in order of lowest-to-highest $fgTiO_2$ SED accumulation
1098 to visually present the wide variation in $fgTiO_2$ cellular loading. Translucent red circle-markers were
1099 placed on thresholded reflectant foci to aid visualisation. **m-p**, Quantitative analysis of the image-
1100 data shown in **a-L**. **m**, Thresholded reflectance per unit tissue area (*i.e.,* amount of $fgTiO_2$ per unit
1101 tissue area). **n**, Thresholded reflectance per cell (*i.e.,* $fgTiO_2$ dose per cell). **o**, Number of thresholded
1102 reflectant foci per cell (*i.e.,* number of $fgTiO_2$-loaded vesicles (TLV) per cell). **p**, Thresholded
1103 reflectance signal per foci (*i.e.,* $fgTiO_2$ dose per TLV). Statistical comparison of the distributions is

1104 presented in **Supplementary Figure 6** (two-sided Wilcoxon rank-sum analysis). None of the
1105 measured $fgTiO_2$ distributions were found to be entirely unique to either species. **m-p**, By all of the
1106 quantitative measures established, feeding a murine diet supplemented with 0.0625% (w/w) $fgTiO_2$
1107 for eighteen weeks provides significant overlap with measured, real-world human exposures. *Scale*
1108 *bars:* ***a-L*** *= 50 µm with insets 10 µm;* ***n*** *= 20 µm;* ***p*** *= 5 µm.*
1109

1110 **Figure 4 – $fgTiO_2$ selectively targets PD-L1$^+$ LysoMac and LysoDC cells. a-h**, *In situ*, single-cell
1111 analysis of key immune-cell subtypes of the mouse subepithelial dome. **a/b**, Example images
1112 immunofluorescently labelled for B220, CD3 and CD11c (*i.e.,* identifying B-lymphocytes, T-
1113 lymphocytes and phagocytic mononuclear cells, respectively) from wild-type (WT) mice fed (**a**)
1114 without (WT) or (**b**) with (WT + TiO_2) $fgTiO_2$ dietary supplementation (0.0625% w/w of diet).
1115 $fgTiO_2$ was measured from thresholded reflectance images. Translucent red circle-markers are placed
1116 on reflectant foci to aid visualisation. **c/d**, Flow cytometry-type plots showing cell area / cell aspect
1117 ratio, (**e-g)** immunofluorescence distributions and (**h**) cell counts for B220$^+$, CD11c$^+$ and CD3$^+$ cells
1118 (n = 3 animals). All measures remained similar regardless of $fgTiO_2$ feeding (cell count comparison
1119 (**h**), P = ≥0.26, two-sided unpaired samples T-tests). **i-L**, $fgTiO_2$-recipient cells of the subepithelial
1120 dome were CD11c$^+$ in ~ 95% of cases. **m-o**, These cells also exhibited a unique, highly
1121 autofluorescent signature as previously-described for subepithelial dome 'lysomac' and 'lysoDC'
1122 mononuclear phagocyte cells. **o**, Again, this was true for almost all fgTiO2$^+$/CD11c$^+$ cells and,
1123 equally, these autofluorescent cells were similarly present in (**n**) controls without $fgTiO_2$ feeding
1124 (further data shown, **Supplementary Figure 8**). **p-u**, Montaged CD11c$^+$/$fgTiO_2^+$ or CD11c$^+$/$fgTiO_2^-$
1125 cell populations from the SEDs of mice fed the $fgTiO_2$ supplemented diet visualised in terms of **(r/s)**
1126 autofluorescence signature. $fgTiO_2$ is seen to both selectively and specifically target the
1127 autofluorescent cells and (**t/u**) the diversity of CD4 and MHCII expression confirms that both

1128 lysomac and lysoDCs take up $fgTiO_2$. **v-z**, $fgTiO_2^+$ cells of the SED expressed the immunotolerance
1129 marker programmed death ligand 1 (PD-L1) whereas $fgTiO_2^+$ pigment cells at the base of the Peyer's
1130 patch tended to lose PD-L1 expression (**y** versus **z**, respectively). **w**, PD-L1 expression in the Peyer's
1131 patches was not significantly perturbed by feeding the $fgTiO_2$-supplemented diet ($P = 0.34$, $z = -0.96$,
1132 two-sided Wilcoxon rank-sum analysis, n = 6 animals). *Scale bars:* ***a/b*** *= 50 μm;* ***i/m, p-u*** *= 10 μm;* ***x***
1133 *= 500 μm;* ***y/z*** *= 10 μm.*
1134
1135 **Figure 5 – $fgTiO_2$-*Salmonella* interactions.** To enable studies of particle adjuvanticity and cell
1136 migration, in "Mouse Study 2", after the 16-week $fgTiO_2$ feeding period all animals were switched to
1137 a normal laboratory chow diet (*i.e.,* without $fgTiO_2$-supplementation) then half were orally
1138 inoculated with attenuated, Δ*aroA-Salmonella*. Tissues were harvested +3 or +28 days after
1139 infection. **a-c**, Confocal reflectance micrographs displayed as z-stack maximum projections showing
1140 immunofluorescent labelling for flagellin (FliC) to detect the Δ*aroA-Salmonella* in the Peyer's patch
1141 SED region. Marked accumulation of both $fgTiO_2$ and Δ*aroA-Salmonella* was observed in
1142 autofluorescent, phagocytic mononuclear cells at the +3 timepoint. **d**, Faecal ELISA studies
1143 confirmed a marked, *Salmonella*-specific IgA response at the +28 timepoint (bars represent medians
1144 with interquartile range error-bars, n = 3-6 samples per treatment group). **e-g**, Protein expression
1145 analyses of ileal tissue digests by proximity extension assay (OLINK mouse exploratory panel). **e,**
1146 Comparison of ileal tissues taken from wild-type (WT) mice unexposed to $fgTiO_2$ but with (WT
1147 +*Sal*) or without (WT) Δ*aroA-Salmonella* infection confirmed significant increases in expression of
1148 key cytokines / chemokines associated with a Th1 immune response ($P \leq 0.026$, two-sided Wilcoxon
1149 rank-sum test, n = 5-6 tissues per group). **f**, Inflammation-associated protein expression analyses of
1150 ileal tissue digests in the WT, WT +TiO_2, WT +*Sal* and WT +TiO_2 +*Sal* treatment groups at the +3
1151 and +28-day timepoints. No significant differences were observed between the WT and WT +TiO_2 (P

1152 ≥ 0.53, two-sided Wilcoxon rank-sum test, n = 3 animals per group) or WT + *Sal* and WT +TiO_2
1153 +*Sal* groups (P ≥ 0.79, two-sided Wilcoxon rank-sum test, n = 6 animals per group). Full dataset is
1154 shown in **Supplementary Figure 12**. **g**, Peyer's patch-focussed inflammation-associated protein
1155 expression analyses using carefully-excised patch digests in mice treated with either Δ*aroA*-
1156 *Salmonella* alone (WT +*Sal*) or with $fgTiO_2$ and Δ*aroA*-*Salmonella* (WT +TiO_2 +*Sal*) at +3 or +28
1157 timepoints. No significant differences were observed between the two groups (P ≥ 0.2, two-sided
1158 Wilcoxon rank-sum test, n = 6 animals per group) at either timepoint demonstrating no interaction of
1159 $fgTiO_2$ and Δ*aroA*-*Salmonella* despite (**a-c**) heavy loading into the same cells (full dataset shown in
1160 **Supplementary Figure 13)**. OLINK protein abbreviations are defined in **Supplementary Table 1**.
1161 *Scale bars:* ***a-c*** *= 10 µm.*
1162
1163 **Figure 6 – Cellular dosimetry of $fgTiO_2$ across timepoints and *Salmonella*-induced migration.**
1164 **a/b/k**, Confocal reflectance micrographs from Mouse Study 2 showing the subepithelial dome (SED)
1165 tissue region (n = 3 animals per group). After the 16-week $fgTiO_2$ feeding period, all animals were
1166 switched to normal laboratory chow diet (without $fgTiO_2$ supplementation) and half were orally
1167 dosed with Δ*aroA*-*Salmonella* before tissue harvest at +3 or +28-day timepoints. **a/b**, In the animals
1168 fed the $fgTiO_2$-supplemented diet without *Salmonella* exposure (WT +TiO_2), $fgTiO_2$-loaded cells
1169 were present in the SEDs at both +3 and +28 timepoints. **c-j**, To gain insights into cellular dosimetry
1170 changes across the two timepoints, quantitative image analysis of complete Peyer's patch transverse
1171 sections was used to precisely measure the number of reflectant foci per-cell (*i.e.,* the $fgTiO_2$-loaded
1172 vesicle (TLV) count per-cell) and the amount of reflectance per foci (*i.e.,* equivalent to the $fgTiO_2$
1173 dose per-vesicle). **d/e**, At the +28 timepoint, the TLV count per-cell was markedly elevated with a
1174 new population of cells with TLV counts >13 forming in the mid-to-base regions of the follicle. **f/g**,
1175 Randomly sampling and montaging the reflectance (RL) information in cells from each of the two
1176 timepoints visually demonstrates this, showing (**g**) more heavily-loaded cells at the +28 timepoint. **h**,

1177 Moving from cell to vesicle information, in contrast, the amount of reflected light per individual foci
1178 remained near-identical across the two timepoints and this was again borne out visually when (**i/j**)
1179 individual TLVs were randomly montaged. Collectively, the results suggest that once fgTiO2-loaded
1180 cells move below the SED, there is a process of vesicular inheritance by certain cells over time,
1181 providing a route to the formation of heavily-loaded pigment cells at the follicle base – as is well-
1182 described in humans (**Figure 1**). **k**, Challenge with Δ*aroA-Salmonella* (WT +TiO_2 +*Sal*) markedly
1183 changed this picture (n = 4 animals per group). At the +28 timepoint, SEDs were almost completely
1184 devoid of both $fgTiO_2$ and autofluorescence-positive cells. Out of four SEDs imaged, only one
1185 reflectant foci was detectable (indicated by arrow) showing marked migration of $fgTiO_2$ from the
1186 SED tissue compartment after Δ*aroA-Salmonella* exposure. *Scale bars:* ***a/b/k*** *= 50 µm,* ***c/d*** *= 250*
1187 *µm,* ***f/g/i/j****, = 10 µm.*
1188
1189 **Figure 7 – Ileal distribution of $fgTiO_2$ following *Salmonella* challenge. a**, Single-cell image
1190 analysis of tilescanned confocal reflectance images collected from transverse sections of mouse ileal
1191 tissue from the $fgTiO_2$-exposed, Δ*aroA-Salmonella*-infected treatment group (+28-day timepoint, n =
1192 3 animals). $fgTiO_2$-positive cells in the Peyer's patches are displayed in red. As in **Figure 6**, the
1193 subepithelial dome (SED) regions were devoid of $fgTiO_2$ with the majority of the positive cells
1194 located basally around the follicle margins. In contrast to all previous data collected without Δ*aroA-*
1195 *Salmonella* exposure, $fgTiO_2$-positive cells (displayed in white) were now also present in the villous
1196 mucosa. Bigger versions of the single-cell analyses presented in (**a**) are available in **Supplementary**
1197 **Figure 15**. **b**, Montaging positive events from villous mucosa regions showed that particle loading
1198 was low compared to Peyer's patch cells with the majority containing single reflectant foci. **c**, High
1199 resolution imaging of optically cross-sectioned villi confirmed reflectant foci deep in the lamina
1200 propria in the same manner as observed in humans (**Figure 1c**). **d**, The majority of the $fgTiO_2$-
1201 positive events in the villous mucosa also displayed the same autofluorescence signature as was

1202 observed in the particle-recipient cells of the SED. *Scale bars:* ***a*** *= 250 µm;* ***b-d*** *= 20 µm.*

1203

1204 **ACKNOWLEDGEMENTS**

1205 The authors acknowledge the UK Medical Research Council (grant number MR/R005699/1), the UK
1206 Engineering and Physical Sciences Research Council (grant EP/N013506/1) and the UK
1207 Biotechnology and Biological Sciences Research Council (grant number BB/P026818/1) for
1208 supporting the work. J.W.W. is grateful to Girton College and the University of Cambridge Herchel-
1209 Smith Fund for supporting him with Fellowships. J.W.W. thanks Debbie Edwards for her assistance
1210 with the microscopy studies and Guy Dew for his comments on the manuscript. The authors thank
1211 Prof. Neil Mabbot and Prof. Simon Milling for their helpful comments. J.D.S. and Å.V.K. were
1212 supported by Swedish Research Council Grant No. 2021-02566. Mouse Study 1 was funded by the
1213 Riddet Institute through its Centre of Research Excellence funding which was awarded by the New
1214 Zealand government. Additional funding was provided by the Ministry for Science and Innovation
1215 contract C11 × 1009 through Nutrigenomics New Zealand, a collaboration between AgResearch,
1216 Plant and Food Research, and The University of Auckland. S.R. was supported by doctoral
1217 scholarships from Massey University. The authors are grateful to Dr. Andrew Grant for his input into
1218 the study design for Mouse Study 2.

1219

1220 **AUTHOR CONTRIBUTIONS**

1221 JWW and JJP conceived the concept and designed the analyses. NR obtained funding for SR Ph.D.
1222 studies including Mouse Study 1. SR, NR and DO carried out Mouse Study 1. RJ, ABDS, MM, CB,
1223 JW, PM and JJP carried out Mouse Study 2. AVK and JDS collected the human surgical specimens.
1224 JWW, JR, MM, AF and REH conducted the light microscopical studies. AD, MM, JWW and JJP
1225 performed the protein expression analyses. APB, SM and JWW carried out the electron
1226 microanalytical work. JWW, PR, HDS and JJP performed the data analysis. JWW and JJP wrote the

manuscript in close collaboration with all authors.

COMPETING INTERESTS

The authors declare no competing interests.